Short Communication

Deciphering the immune modulation through deep transcriptomic profiling and therapeutic implications of DNA damage repair pattern in hepatocellular carcinoma

Weifeng Hong [a,1], Yang Zhang [a,1], Siwei Wang [a,1], Danxue Zheng [a], Shujung Hsu [a], Jian Zhou [b], Jia Fan [b], Zhaochong Zeng [a], Nan Wang [c], Zhiyong Ding [c], Min Yu [d,**], Qiang Gao [b,***], Shisuo Du [a,*]

[a] Department of Radiation Oncology, Cancer Center, Zhongshan Hospital, Fudan University, Shanghai, 200000, China
[b] Department of Liver Surgery and Transplantation, Key Laboratory of Carcinogenesis and Cancer Invasion (Ministry of Education), Liver Cancer Institute, Zhongshan Hospital, Fudan University, Shanghai, 200032, China
[c] Mills Institute for Personalized Cancer Care, Fynn Biotechnologies Ltd., Jinan, Shandong, 250000, China
[d] Department of Pancreas Center, Guangdong Provincial People's Hospital, Guangdong Academy of Medical Sciences, Southern Medical University, Guangzhou, Guangdong, 510000, China

ARTICLE INFO

ABSTRACT

Aims: DNA damage repair (DDR) plays a pivotal role in hepatocellular carcinoma (HCC), driving oncogenesis, progression, and therapeutic response. However, the mechanisms of DDR mediated immune cells and immuno-modulatory pathways in HCC are yet ill-defined.

Methods: Our study introduces an innovative deep machine learning framework for precise DDR assessment, utilizing single-cell RNA sequencing (scRNA-seq) and bulk RNA-seq data. Single-cell RNA sequencing data were obtained and in total 85,628 cells of primary or post-immunotherapy cases were analyzed. Large-scale HCC datasets, including 1027 patients in house together with public datasets, were used for 101 machine-learning models and a novel DDR feature was derived at single-cell resolution (DDRscore). Druggable targets were predicted using the reverse phase protein array (RPPA) proteomic profiling of 169 HCC patients and RNA-seq data from 22 liver cancer cell lines.

Results: Our investigation reveals a dynamic interplay of DDR with natural killer cells and B cells in the primary HCC microenvironment, shaping a tumor-promoting immune milieu through metabolic programming. Analysis of HCC post-immunotherapy demonstrates elevated DDR levels that induces epithelial-mesenchymal transition and fibroblast-like transformation, reshaping the fibrotic tumor microenvironment. Conversely, attenuated DDR promotes antigen cross-presentation by dendritic cells and CD8$^+$ T cells, modulating the inflammatory tumor microenvironment. Regulatory network analysis identifies the CXCL10-CXCR3 axis as a key determinant of immunotherapeutic response in low DDR HCC, potentially regulated by transcription factors GATA3, REL, and TBX21. Using machine learning techniques by combining bulk RNA-seq data in house together with public datasets, we introduce DDRscore, a robust consensus DDR scoring system to predict overall survival and resistance to PD-1 therapy in HCC patients. Finally, we identify BRAF as a potential therapeutic target for high DDRscore patients.

Conclusion: Our comprehensive findings advance our understanding of DDR and the tumor microenvironment in HCC, providing insights into immune regulatory mechanisms mediated via DDR pathways.

---

* Corresponding author.
** Corresponding author.
*** Corresponding author.
E-mail addresses: yumin@gdph.org.cn (M. Yu), gaoqiang@fudan.edu.cn (Q. Gao), du.shisuo@zs-hospital.sh.cn (S. Du).
[1] Weifeng Hong, Yang Zhang and Siwei Wang contributed equally to this work.

1. Introduction

Genomic instability caused by defects in DNA damage repair (DDR) is regarded as an important hallmark in multiple cancers [1,2]. Previous clinical trials have revealed the combinatory benefit of cisplatin with radiation therapy to achieve longer progression-free survival (PFS) by three years in patients with locally advanced uterine cervical or vaginal cancers [3]. Mechanistically, DDR influences multiple aspects of tumor immunogenicity, including tumor cell-autonomous responses and tumor cell–microenvironment interactions. The efficacy of anti-programmed death 1 (anti-PD1)/anti-programmed death ligand 1 (anti-PD-L1) immune checkpoint inhibitors (ICI) in treating mismatch repair (MMR)-deficient (MMRd) tumors regardless of histology, already sets the function of such interplay [4,5]. More recently, targeting the DDR pathway has been proposed as a promising therapeutic strategy to induce anti-tumor immunity [6–8]. This led to a few exploratory clinical trials to evaluate potentials of incorporating DNA-damaging or DDR-targeting agents with ICI [9]. DDR inhibitors combined with immunotherapy have garnered a growing amount of interest. In principle, DDR inhibition activates the STING/TBK1/IRF3 innate immune pathway, increasing CXCL10 and CCL5 levels in turn evoking cytotoxic T cells to eradicate malignant cells [10]. Supporting evidence from clinical trials involving ICI treatment have further revealed DDR-related biomarkers to potentially predict ICI response [11]. Therefore, elucidating the alterations and interaction mechanisms of DDR pathway genes is of great significance in exploring the role of DDR in cancer therapy.

In recent years, mutational landscapes established on hepatocellular carcinoma (HCC) via whole-genome sequencing (WGS) profiles have uncovered the relationship between DDR gene mutations and altered cellular responses under various DNA damage conditions and some of which caused the accumulation of driver mutations to induce global genomic instability and thereby facilitating tumorigenesis and cancer progression [12,13]. DDR pathway alterations also affect immunotherapy efficacy. Indeed, genomic instability featured by elevated mutation frequencies results in dysregulation in the DDR pathway causing a high mutational load linking with an increase in neoantigen load (NAL) and tumor-infiltrating lymphocytes (TILs), a key hallmark to sensitize with ICI [14,15]. In such, mutations in DDR genes can upregulate NAL, $CD4^+$ T cells, and $CD8^+$ T cells, and alter PD-1 and PD-L1 expression [16, 17]. Although immunotherapy with atezolizumab plus bevacizumab was the first regimen to demonstrate superiority over sorafenib monotherapy in a randomized phase III trial and was approved as a standard first-line treatment for advanced HCC by the Food and Drug Administration (FDA), only a minority of patients experience clinical benefits [18]. Therefore, a deeper comprehension of the interaction between the TME and the DDR as well as the dynamic immune ecosystem under various DDR statuses will be valuable to resolve the heterogeneity and relevant mechanisms through the innate immune response in HCC and may help developed more effective treatment strategies.

In this study, we incorporated multi-omics analyses, including scRNA-seq, bulk RNA-seq (tissue and cell lines) and targeted proteomics (reverse phase protein arrays, RPPA), to comprehensively address the molecular heterogeneity of the tumor microenvironment (TME) in HCC under different DDR statuses induced by immunotherapy. Using a sophisticated combination of machine learning algorithms, we established an RNA sequencing-based DDR scoring framework termed DDRscore. By integrating this DDR scoring framework with proteomics and cell line RNA-seq data, we successfully identified potential therapeutic targets (BRAF) specifically tailored for high DDR status in HCC.

2. Methods

2.1. Patient sample acquisition and approval

This study was approved by the Ethics Committee of Zhongshan Hospital, Fudan University, China (B2022-048R). In total 170 HCC patients with paired tumors and adjacent nontumor liver tissues were included in this analysis (159 HCC patients for RNA-seq analysis and 11 HCC patients for RPPA (FDUZS, Table S1)). All patients undergoing primary curative resection at Zhongshan Hospital were treatment-naïve. All tissue samples were preserved within 30 min after surgery to ensure the quality for downstream profiling.

2.2. External data collection

We used two sets of external scRNA-seq data (GSE149614 [19] and GSE151530 [20]), which were pre-annotated in details with sufficient clinical information. We also downloaded three bulk-seq cohorts to examine the robustness and clinical value of DDRscore and those included 349 individuals from The Cancer Genome Atlas (https://portal.gdc.cancer.gov/) TCGA-LIHC cohort, 196 individuals from the International Cancer Genome Consortium (https://dcc.icgc.org/) ICGC LIRI-JP cohort, and 312 individuals from the previously published study by Choueiri et al. [21]. Transcriptome data were processed by log2 transformation from transcripts per million values (TPM). A collection of 276 genes associated with DDR were compiled from previously published studies. The Cancer Proteome Atlas (https://tcpaportal.org/tcpa/) provided protein array (RPPA) information for 169 HCC cases. Expression profiles of 22 hepatocellular carcinoma cell lines were received from the Broad Institute Cancer Cell Line Encyclopedia (CCLE) project (https://portals.broadinstitute.org/ccle/). From genome-scale CRISPR knockout screening, the CERES scores of 18,333 genes in 739 cell lines were obtained from the Cancer Dependency Map (https://depmap.org/portal/). CERES scores were used to quantify the dependence of the desired gene on specific tumor cell lines (CCLs), with lower scores suggesting that the gene is more likely to be required for proliferation and survival in the given CCLs.

2.3. Preprocessing and analysis of scRNA-seq data

2.3.1. Data pre-processing, filtering and normalization

Two scRNA-seq datasets from above were processed separately using Seurat v4. For the GSE149614 cohort, cells with 500 to 6000 genes and 1000 to 100,000 UMIs were pre-selected based on their expression profiles. The filtering criteria included a mitochondrial gene fraction of less than 15 %. Similarly, for the GSE151530 cohort, cells with 300 to 8000 genes and 1000 to 80,000 UMIs were selected. The filtering criteria for this cohort were a mitochondrial gene fraction of less than 30 %. Post-selection, both datasets were re-normalized using Seurat's SCTransform, and the top most 3000 genes were selected as highly variable genes (HVG) and utilized to stabilize UMI count variance.

Clustering and cell type annotation. The principal component analysis (PCA) was performed using highly variable genes (HVGs), and the shared nearest neighbor (SNN) graph and unified manifold approximation and projection (UMAP) were constructed using Louvain algorithm by selecting the first 30 principal components and clustering units. For the GSE149614 cohort, the major cell types were identified based on cross-cohort typical cell type-labeled scores: Hepatocytes were labeled with ALB, EPCAM, SERPINA1, and HNF4A; B cells were labeled with CD19, CD79A, and MS4A1; CD4, CD3D, CD3E, and TRAC were used to identify $CD4^+$ T cells; and CD8A, CD8B, and GZMK were used to identify $CD8^+$ T cells; Natural killer cells (NKs) were labeled with GNLY and NKG7; dendritic cells were labeled with C1orf54, LGALS2, CD1C, and XCR1; macrophages were labeled with CD68, FCGR1A, and ITGAX; endothelial cells were labeled with CDH5, CLDN5, and RAMP2; and fibroblasts were labeled with C1R, COL1A2, and DCN.

To predict copy number alteration without tumor annotations, we used the CopyKAT (https://github.com/navinlabcode/copykat) [22] to define the aneuploid cell cluster.

We follow the walkthrough (https://satijalab.org/seurat/v3.1/integration.html) to perform Reference Mapping on GSE151530 cohort based

on GSE149614 cohort. As described in the original publication, we here specify GSE149614 cohort as the "reference" possibility for integration analysis, and GSE151530 cohort is designated as the "query". original publication, we here specify GSE149614 cohort as the "reference" possibility for the integrated analysis, and GSE151530 cohort is specified as the "query" dataset. dataset. The process was accomplished using the TransferData algorithm [23].

For subcluster analysis of B cells and NKs, the clustree package was used to select the resolution [24]. FindAllMarkers function was utilized to find genes with differential expression, and the FindMarkers function was used for comparative analysis of conditions within each cluster.

2.4. High-dimensional weighted gene Co-expression network analysis (hdWGCNA)

Co-expression analysis for single cell RNA-seq was accomplished using the accessible R package hdWGCNA (https://github.com/smorabit/hdWGCNA) [25]. According to the manufacturer's description, the method employs a one-step network creation and module recognition method, calculating and displaying module-specific gene expression, adjacency matrix heatmaps, and other pertinent outputs.

2.5. Assessment of DDR status based on scRNA-seq

We applied an algorithm [26,27] which analyzed changes in the signal-to-noise ratio between genes and cells based on the expression profile of DDR-related genes to estimate the capacity of DNA damage repair activity in cells or samples. Specifically, we first normalized the scRNA-seq data from malignant cells only using Seurat to obtain an expression matrix M and calculated the mean expression value E_i for each gene i. Then, using a random sampling approach, all genes were sorted into 50 expression bins due on their E_i, and the frequency of occurrence of DDR-related genes, designated as B_f, was calculated. Random feature genes were selected from each bin based on the B_f count from random sampling, with the overall quantity of random feature genes being equal to the number of DDR-related genes. This random process was iterated 1000 times. Last but not least, a gene centralized expressed matrix was constructed, which can be read as data devoid of excessive migratory signals:

$$Z_{i,j} = M_{i,j} - \left(\sum_j M_{i,j} \right) \Big/ N$$

Where $Z_{i,j}$ is the central expression of gene i in cell j, $M_{i,j}$ is the expression of gene i in cell j in the expression matrix M, and N is the number of cells. Using the central expression matrix, we defined the difference between the average value of the K × 1000 randomly sampled signatures and the average value of K DDR-related genes as the DDRscore for the malignant cells. The pseudo-value of the DDRscore for each cell in each sample is defined as the sample's DDRscore.

2.6. Distribution preference of cell types categories

To describe the distribution of cell types in DDR groups, odds ratios (ORs) were computed and preferences were shown [28]. For each possible combination of cell type i and category j, a 2 × 2 table of contingencies was formed. Then, the OR and corresponding *P*-value were then calculated using Fisher's exact test on the contingency table. Using the Benjamini-Hochberg (BH) approach provided in the R function P. adjust, the *P*-value was modified. A greater OR value implies that cell type i is more likely to be present in tissue j, whereas a smaller OR value suggests that cell type i is less likely to be present in tissue j.

2.7. Function enrichment analysis and trajectory analysis

The activity scores of 14 pathways related to tumorigenesis and

development were calculated using the functional genomics tool, PROGENy [29]. PROGENy evaluates pathway activity using "footprint gene sets", which don't include pathway members but instead include the most sensitive genes to pathway perturbations. Heatmaps were created using the ComplexHeatmap [30]. Gene set enrichment analysis (GSEA) was performed on the enrichment process of the cell clusters using the clusterProfiler [31]. To reveal the potential relationship between malignant cells and fibroblasts, a trajectory analysis was performed using Monocle v2 [32]. Using the differalgenetest function, significant genes (BH-corrected P 0.01) were identified and the cells were sorted in an unsupervised way during the differential expression analysis of the investigated cells. Dimension reduction and cell sorting were performed with default parameters followed by trajectory construction.

2.8. Cell-cell communication

In order to study the potential interactions between cell types in the TME with different DDR scores after receiving ICIs in HCC, we used CellPhoneDB for cell-cell communication analysis [33]. We started by randomly shuffled the clusters labelling of all cells 1000 times to calculate the mean ligand and receptor expression levels of the interaction clusters. This resulted in a distribution of zero for every receptor-ligand pair. We determined the theoretical *P*-value of cell type specialization for each receptor-ligand complex by calculating the fraction of average values greater than the actual average value. Then, we chose interactions of biological relevance. To further understand the gene expression pattern differences under different DDR scores, we used the NicheNet method to predict which ligands regulate which receptors in the expression of another cell type that is formed by one cell type.

2.9. "Ligands – receptors - transcription factors - target genes" regulatory network

The interplay between dendritic cells (DCs) and CD8$^+$ T cells under low DDR conditions was analyzed using scMLnet package [34]. ScMLnet package can simulate not only cell-cell communication but also gene regulation networks within cells. It integrates cell-cell pathways (ligands-receptors interaction) and cell-intracellular sub-networks (receptors-transcription factors pathways and transcription factor-target genes interaction) in accordance with cell type specific gene expression, prior networking knowledge, and parameter estimation. We used scMLnet package to extract the connection data for the "ligands-receptors-transcription factors-target genes" regulatory network. Then, using the iGraph package in the R, we performed network analysis on the extracted data to highlight the neighborhood network and generate enriched biological/pathway terms. Using the clusterProfiler package [31], a gene set enrichment analysis of was conducted.

2.10. Signatures constructed from a combined approach of bulk-seq data and machine learning

To design a consensus DDRscore with desired accuracy and reliability, we tested our data against 10 machine learning methods with 101 algorithm combinations [35]. Those algorithms include Random Survival Forest (RSF), Elastic Net (Enet), Lasso, Ridge, Stepwise Cox, CoxBoost, Cox Partial Least Squares Regression (plsRcox), Supervised Principal Component (SuperPC), Generalized Boosted Regression Model (GBM), and Survival Support Vector Machine (survival-SVM). Firstly, DDR-related genes congruent with scRNA-seq data were included in 101 algorithm combinations to train prediction models in the TCGA-LIHC cohort using leave-one-out cross-validation (LOOCV). Then, all models were validated in the ICGC LIRI-JP cohort. Ultimately, the Harrell consistency index (C-index) was computed for all training and validation sets for each model, and the model with the greatest average C-index was chosen as the best model. Meanwhile, survival modeling and

Kaplan-Meier (KM) analysis were conducted using the "survival" package in R.

2.11. Reverse phase protein arrays and data processing

For RPPA proteomics, each specimen was evaluated by a committee-certified pathologist (H&E-stained slide) to confirm the histology and tumor contents. Protein quality control and examination samples (protein level >1.5 μg/μl) will undergo rigorous progressive dilution with Tecan Fluent 480/780 (1, 1/2, 1/4, 1/8, 1/16). More than 400 protein microarrays were generated using the Quanterix 2470 Arrayer high-speed printing workstation. Using the Cancer Signaling Pano-Profiler, 384 antibodies in this panel were colorimetrically visualized on the microarray chip (one antibody to one slide) using the Agilent Autostainer Link 48 automatic staining system. Following colorimetric development, the Huron TissueScope LE120 high-throughput slide scanner was used for high-resolution readout acquisition. MicroVigene analytics software was then used for digital conversion of image data into quantitative data (raw data defined as level 1 data L1) based on the predefined pixel intensity algorism [36]. Raw data were linear transformed to general level 2 data (L2), Data were then normalized by median-centering across all proteins and then centered across all samples to generate comparable data for plotting.

2.12. Drug target and agents' response analysis

We downloaded 2249 target information for 6125 compounds from a published study to search for candidate druggable targets [37]. To identify protein targets with promising clinical importance in HCC patients with high DDRscore, a Spearman correlation analysis was conducted between the RPPA protein expression data and DDRscore. Proteins with a correlation coefficient greater than 0.3 were considered drug targets associated with poor prognosis. Following this, we generated the DDRscore with each liver cancer cell line from the CCLE project and ran a correlation analysis between the DDRscore and the CERES score on these cell lines. CERES is a method that estimates gene dependence while considering copy number effects during essential screening, a method previously applied to the Avana dataset to calculate the CERES score for each gene and cell line [38]. The lower the CERES score, the higher the likelihood that the gene is dependent on a specific CCL. Thus, we considered genes with a correlation coefficient less than -0.25 as drug targets associated with poor prognosis. The targets identified using both of methods were considered as potential therapeutic drug targets for HCC with high DDRscores. To predict drug response, logistic regression methods (including ridge regression and elastic nets) were applied [39]. For ridge regression, prophet package in R was used [40] to test the performance of the drug response predictive accuracy using default 10-fold cross-validation in clinical specimens.

2.13. Statistical analysis

R software (version 4.2.1) and Python (version 3.9.12) were utilized for all statistical analyses. If the variables were normally distributed, parametric tests (Student's t-test or ANOVA) or for data exhibiting non-normality, non-parametric tests (Wilcoxon rank-sum test or Kruskal-Walli's test) were used to compare continuous variables between two or more groups. Pearson's r correlation or Spearman's rank-order correlation were used to measure the relationship between two continuous variables.

3. Results

3.1. DDR heterogeneity analysis of malignant cells in HCC

To perform an in-depth analysis of the interplay between malignant cells and the TME in HCC associated with different DDR conditions, we collected two single-cell RNA-seq datasets. The GSE149614 dataset contained 9 benign livers tissues and 10 HCC tissues, while the GSE151530 dataset contained 4 HCC tissues without immune checkpoint inhibitor (ICI) treatment and 9 HCC tissues that were treated with ICI. All these patients were characterized with various stages according to American Joint Committee on Cancer (AJCC) (Table S2). Meanwhile, bulk RNA sequencing (bulk-RNA seq) datasets were employed to test against 101 machine-learning models including 159 patients from our own cohort (FDUZS), 349 patients from the TCGA-LIHC cohort, 243 patients from the ICGC-LIRI-JP cohort, and 312 patients from the cohort of Choueiri et al. In addition, reverse-phase protein array (RPPA) data from 169 HCC patients and bulk-seq data from 22 liver cancer cell lines were utilized to develop therapeutic targets and predict prospective treatments. Finally, 11 pairs of HCC and adjacent normal tissues were subject to RPPA proteomic profiling, and results were validated in TCGA HCC cohort. The schematic diagram of this study was depicted in Fig. 1A.

In total, high-quality transcriptome data of 50,920 cells, including 21,140 cells from non-tumor live tissues and 29,780 cells from HCC tissues, were acquired from the GSE149614 dataset after quality assurance and filtering for individual cells. After removal of unwanted cells and data merging, dimension reduction characterized heterogeneity across various tissues, samples, pathological stages (Figs. S1A–D). We noted biological differences in some tumor- or patient-specific clusters indicating potential underlying mechanisms (Figs. S1A–D). To reveal which cellular compartments contributed most to the interpatient heterogeneity, we annotated and partitioned each cell cluster using marker genes. The HCC ecosystem composition was mainly featured by hepatocytes, B cells (BCs), CD4$^+$ T cells (CD4s), CD8$^+$ T cells (CD8s), natural killer cells (NKs), dendritic cells (DCs), macrophages, endothelial cells (ECs), and fibroblasts (Fibs) (Fig. 1B). To further resolve the intertumoral heterogeneity, we compared the contents of the cellular compartments at individual sample levels (Fig. 1C). Despite being heterogenous at inter-sample scale, epithelial and immune cells showed a distinct tissue-of-origin difference between normal and cancerous tissues. Immune cells were predominant in para-tumor samples, whereas HCC tissues had significantly expanded malignant epithelium, probably due to the growing malignant cells in tumor samples (Figure S1E, Figure S1F). Though enlarged tumor contents existed by large during oncogenic transformation, this seemed also associated with difference tumor stages (Fig. S1F right panel and S1G right panel). Of the immune components, B cells and T cells experienced significant alterations during tumor progression, whereas the liver resident macrophages remained almost unchanged (Figure S1G, Figure S1F).

Upon obtaining the basic HCC TME characteristics, we applied the CopyKAT algorithm to assess large-scale chromosomal copy number alterations by focusing on liver cancer cells exclusively. We extracted 9957 malignant cells identified from 9 tumor samples containing at least 50 malignant cells and retained for further analysis (one sample discarded due to low malignant cell numbers identified) (Fig. 1D). Intertumoral heterogeneities were observed highlighting pre-existing biological differences of malignant cells stemming from sample-of-origins (Fig. 1E, left panel). In addition, the frequency of the identified malignant cell populations varied between samples, which were shown to form clusters essentially according to the pathological stages by the dendrogram (Fig. 1E, right panel). To quantify the DDR status of malignant cells, we first performed high-dimensional weighted gene co-expression network analysis (hdWGCNA) on the single-cell expression profiles of 9957 malignant cells to extract genes linking with oncogenic transformation. We identified 19 gene modules under an optimal scale-free topology model fit with a soft threshold of 5 (Fig. S2). For each module, we also constructed co-expression networks based on individual module gene profiles (Fig. S3). Notably, most of the hub genes in module 3 belonged to the ribosomal protein family, whose expression has been implicated in the onset and progression of malignancies corroborating the trueness of identified genes via hdWGCNA [41]. Next,
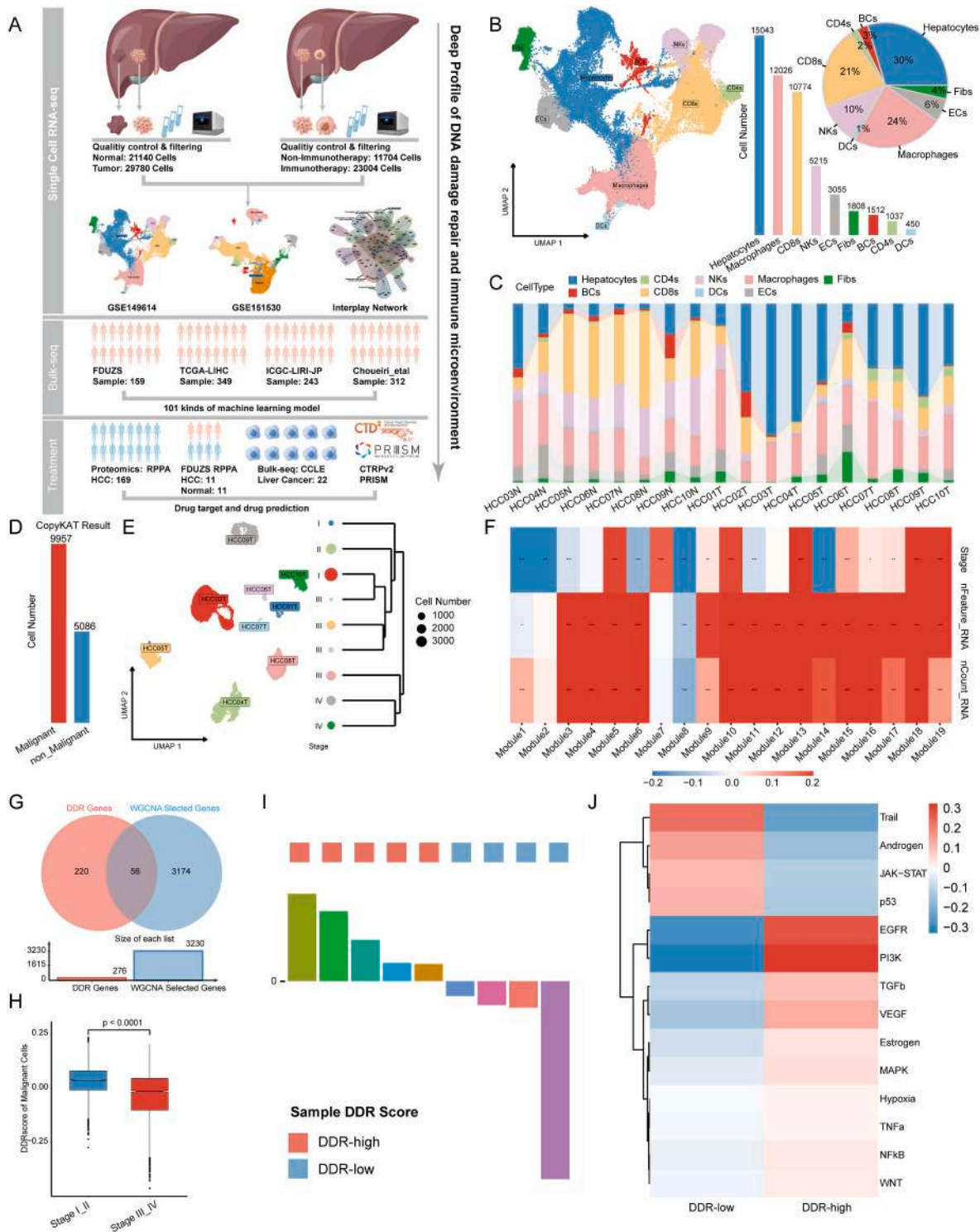
Fig. 1. DDR Heterogeneity in Malignant Cells. A. Workflow for experimental design and analysis. B. UMAP plot (left panel), bar plot representing cell numbers (middle panel), and pie chart representing cell proportions (right panel) based on 50920 filtered cells, with each color indicating the associated cell type. C. Relative percentages of 9 cell populations in different sample sources. D. Number of CopyKAT-identified malignant and non-malignant cells. E. UMAP plot of 9957 malignant cells (left panel) and hclust tree plot of corresponding clusters from different samples (right panel), with each color representing the related sample source and the size of the circle representing the number of cells. F. WGCNA analysis. Phenotypic characteristics are displayed on the right of the image, and the bottom of the image represents different gene modules. G. Venn diagram (top panel) and bar plot (bottom panel) showing the intersection of the DDR gene set and the genes selected by WGCNA and their numbers. H. Differences in DDR in malignant cells at different stages. The statistical differences between groups were determined by the Wilcoxon rank test. I. Bar graph of the DDRscore for each HCC sample. J. PROGENy calculates the activity scores of 14 pathways related to tumor initiation and development in the DDRscore group. $P < 0.05$, **$P < 0.01$, ***$P < 0.001$.

we selected total of 3230 genes significantly associated with the TNM stage from all identified modules as key indicators of tumor progression (Fig. 1F). Within that, 56 genes were known to be involved in the DDR process (Fig. 1G). In order to build a quantitative model to infer DDR status according to clinical stages, we used those 56 shared genes and a parameterized scoring system (DDRscore) was then developed which allowed quantitative assessment DDR status based on malignant cells. By applying the DDRscore scoring system, we found early HCC had significantly higher levels of the DNA damage repair activity as compared to late-stage HCC (p < 0.0001, Fig. 1H) supporting the previous hypothesis whereby loss of efficient DNA repair machinery induces cumulating mutations and subsequent genetic instability along with tumor progression [42]. The overall DDR levels of HCC samples were derived using the DDRscore of malignant cells. Samples with DDR levels greater than 0 were defined as the "DDR-high" group, while those with DDR levels less than 0 were defined as the DDR-low group (Fig. 1I). Under this grouping assignment, we compared relevant pathways to differentiate those tumor cells based on gene enrichment analysis and
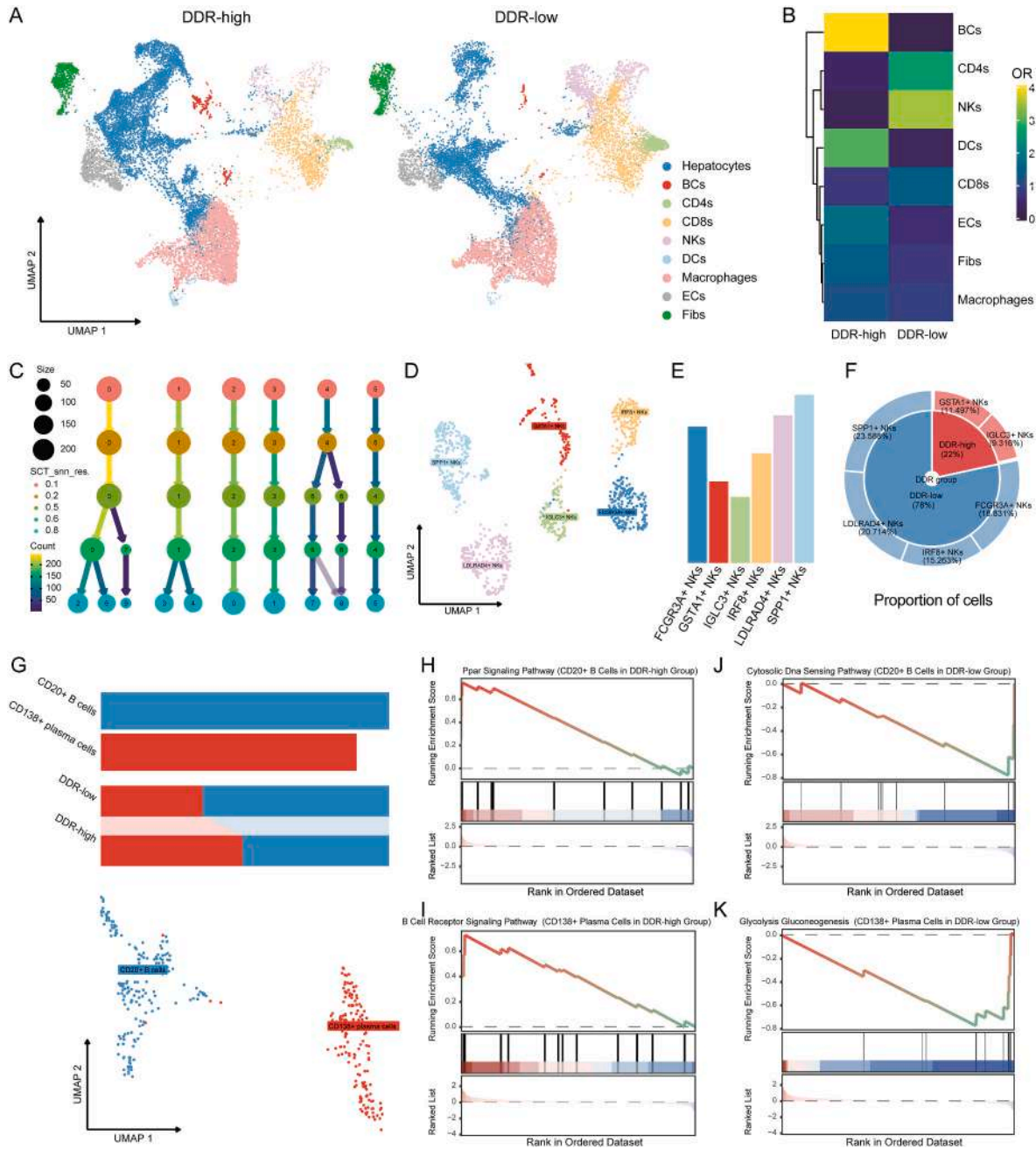

Fig. 2. Analysis of the tumor microenvironment in HCC with different levels of DDR using scRNA-seq. A. UMAP visualization of the HCC tumor microenvironment in different DDRscore groups, with each color indicating the associated cell type. B. Heat map showing the occurrence of cellular clusters with OR in each group. OR > 1.5 indicates that the cell cluster is preferentially distributed in the corresponding group. Hierarchical clustering based on cosine distance is applied to the rows. C. Clustree plot of unsupervised clustering at different resolution values. D. UMAP visualization of natural killer cells, with each color representing the corresponding subcellular type. E. Bar graph showing the number of the 6 subtypes of natural killer cells. F. Pie chart showing the relative proportions of the two DDRscore groups and the 6 subtypes of natural killer cells. G. Bar graph (top panel) showing the number of the two B cell subtypes, a relative proportion chart (middle panel), and UMAP visualization (bottom panel), with each color representing the corresponding subcellular type. H–K. GSEA showing the key enriched pathways in the DDR-high high and DDR-low groups for the two B cell subtypes.

found 14 classical tumor-associated pathways. In particular, those included up-regulated anti-tumoral p53 and tumor necrosis factor-related apoptosis-inducing ligand (TRAIL) pathways enriched in the low DDR group whereas pro-tumor epidermal growth factor receptor (EGFR) and phosphatidylinositol 3-kinases (PI3Ks) pathways were up-regulated in the high DDR group validating our DDRscore classification (Fig. 1J). Taken together, these results suggested that the DDR of malignant cells has significant intertumoral heterogeneity and may contribute to tumor progression.

3.2. Distinct profiles of the TME ecosystem in HCC under varying DDR conditions

Upon elucidating the DDR-driven tumorigenic alteration, we continued to explore the difference from TME perspective across HCC samples. According to patient level DDR assignment, we generated both DDR-high and DDR-low TME at single cell resolution (Fig. 2A). We applied odds ratio (OR) based statistical analysis to evaluate potential cell type alterations. Interestingly, while NK cells had the strongest association with the "DDR-low" group, B cells appeared to be enriched most in the "DDR-high" group (Fig. 2B). By focusing on NKs sub population, we generated a classification free. We then dissected further in details of those heterogenous cell clusters. For NK cells, single-cell expression profiles (including both DDR-high and DDR-low tumors) were clustered under various resolutions, and a classification tree was subsequently constructed. Results indicated a stable region within this tree (resolution 0.1–0.5, Fig. 2C). NKs were clustered into six subsets: SPP1$^+$ NKs, LDLRAD4$^+$ NKs, GSTA1$^+$ NKs, IGLC3$^+$ NKs, IRF8$^+$ NKs, and FCGR3A$^+$ NKs (Fig. 2D–E). Within those NK subsets, the majority (78 %) belonged to the "DDR-low" group and these mainly contained SPP1$^+$ NKs, LDLRAD4$^+$ NKs, IRF8$^+$ NKs, and FCGR3A$^+$ NKs. Oppositely, the "DDR-high" group were dominated by GSTA1$^+$ NKs and IGLC3$^+$ NKs (Fig. 2F). Highly expressed FCGR3A in NKs (FCGR3A$^+$ NKs) is an essential receptor for triggering antibody-dependent cytotoxicity, promoting NKs proliferation, and memory-like cytotoxicity against cancer cells [43]. Meanwhile, GSTA1, as a marker gene of GSTA1$^+$ NKs, is related to tumor susceptibility and the metabolic process [44]. Furthermore, by applying enrichment analyses on those subsets, we showed that both FCGR3A$^+$ and LDLRAD4$^+$ NKs were involved in the antigen processing and presentation-related pathways of endopeptidase indicating a more dynamic immune activity in DDR-low group. Besides, SPP1$^+$ NKs were likely to be involved in processes such as "response to unfolded protein" whereas GSTA1$^+$ NKs associated with DDR-high group had more active metabolic process such as the "fatty acid metabolic processing". (Fig. S4A).

Regarding the B cells, we also dissected them into CD20$^+$ B Cells and CD138$^+$ plasma cells (Fig. 2G lower panel). Notably, CD20$^+$ B Cells were more prevalent in the "DDR-low" group as compared to the "DDR-high" group (Fig. 2G, upper panel). Moreover, the presence of CD20$^+$ B Cells in the "DDR-low" group featured highly expressed CXCL8 and GZMB indicating a probable synergistic response of tumor-infiltrating CD20$^+$ B Cells with cytotoxic T lymphocytes to restrain tumor progression (Fig. S4B) [45]. Pathway analysis indicated CD20$^+$ activates "PPAR signaling pathway" in the "DDR-high" patients, whereas the "cytoplasmic DNA sensing pathway", namely the cGAS-STING pathway, was more active in the "DDR-low" patients. For CD138$^+$ plasma cells, "DDR-high" group also had elevated "B cell receptor signaling" activity, while "Glycolysis Gluconeogenesis" were enhanced in the "DDR-low" group (Fig. 2H–K). Collectively, our findings supported a NKs and B cells regulated HCC oncogenic switch from efficient DNA repair condition (DDR-high) to a functionally impaired status (DDR-low) by reprogramming the immune ecosystem and metabolic processes.

3.3. Characteristics of high DDR-mediated immunosuppression after immune checkpoint blockade

Since distinct immune regulatory pattern was observed under different DDR status in HCC, we then sought to further explore the relation of DDR in response to immunotherapy response. Using the single cell dataset (GSE151530), we subset a total of 34,708 cells with high-quality transcriptome data, including 11,704 cells from HCC tissues without immunotherapy and 23,004 cells from HCC tissues receiving immunotherapy treatment (anti-PD-1 blockade). After normalization, cells were clustered and inter-group annotations suggested negligible batch effects across samples, sequencing platforms, pathological stages, and treatment groups (Fig. S5A). To uncover the key cellular components contributing towards immunotherapy-induced biological difference, we first annotated cell types using the "TransferData" algorithm by referencing from the cell types deduced from aforementioned sing cell data (GSE149614). This projection allowed identification of epithelial cells included malignant and non-malignant cells and major immune and stromal cells included B Cells, CD4$^+$ T cells, CD8$^+$ T cells, NK cells, dendritic cells, macrophages, endothelial cells, and fibroblasts (Fig. 3A). Patients receiving immunotherapy were mainly with advanced HCC (stage IV) as determined by clinical regimes (Fig. S5A). Compared to normal epithelium, malignant cells expressed genes such as FGA and SDC1 (Fig. S5B). Dendritic cells (DCs), which are involved in antigen presentation, express major histocompatibility complex (MHC) molecules and are responsible for the cross-priming of anti-tumor CD8$^+$ T lymphocytes. Specifically, GZMK was substantially expressed in CD8$^+$ T cells, while TRAC was elevated in CD4$^+$ T cells (Fig. S5B). In addition, the immunotherapy group had fewer malignant cells and more CD8$^+$ T cells compared to the non-immunotherapy group (Fig. 3B). Upon ensuring the robustness of the cell annotation and clustering, we noted the overall HCC neoplastic epithelial ratio had decreased following immunotherapy treatment, a finding likely to be attributed to immune checkpoint inhibitor-induced tumor killing (Fig. 3B–C). UMAP was used to reduce dimensionality and cluster malignant cells. Similar to non-immunotherapy-treated HCC, H08, H68, and H74 all displayed considerable intertumoral heterogeneity (Fig. 3D). In contrast, other malignant cells of HCC receiving immunotherapy (H73a/b, H58a/c, H77, H08 and H74) were relatively close to each other implicating a reduced heterogeneity across samples (Fig. 3D).

Next, we explored the DDR status within those ICI-treatment samples by employing the DDRscore algorithm developed from above. Similarly, samples with DDR levels greater than 0 were classified into the "DDR-high" group, and samples with DDR levels less than 0 were pinned into the "DDR-low" group. At the patient level, different DDR status formed distinct TME with some altered immune phenotype compositions (Fig. 3E). In such, the "DDR-high" group was characterized by elevated malignant tumor cells with reduced infiltration of CD8$^+$ T cells and NKs as compared to "DDR-low" group, a finding not only consistent with above hypothesis but also indicative of existing connection with ICI therapy. We further performed differential and functional analysis on the malignant cell population stratified by DDR status. We observed "DDR-low" group had activated fatty acid metabolism pathway, WNT pathway activation and probable oncogenic MYC activation (Fig. 3F–G). Conversely, "DDR-high" group was signified by epithelial-mesenchymal transition (EMT), oncogenic activation of KRAS matching with above findings (Fig. 3E). Next, to explore how EMT mediates the DDR transition, we plotted the tumor cell development trajectory. Pseudo-time inferred a development tendency starting with malignant cell clusters and gradually differentiating into fibroblasts suggesting a probable role of fibrotic TME formation under DDR-competent conditions (Fig. 3H). Finally, we investigated the immune cell components across patients with varying DDRscore. By analyzing key regulatory molecules within immune-regulatory pathways, a general trend of immune inflammation was observed in DDR-low patients. Those included multiple immune inhibitory checkpoints: CD274, PDCD1, CTLA4, LAG-3, IDO1 and TIGIT.
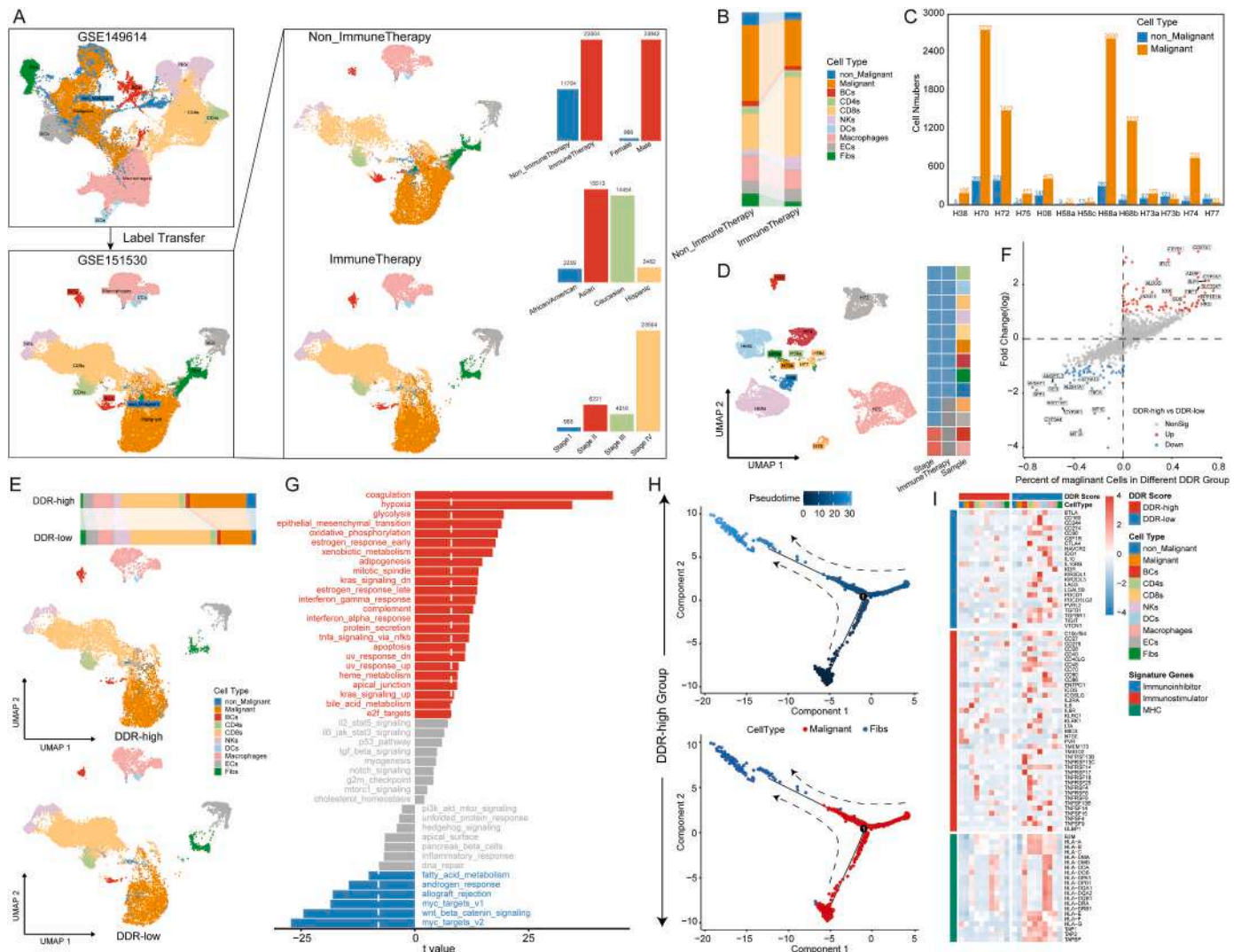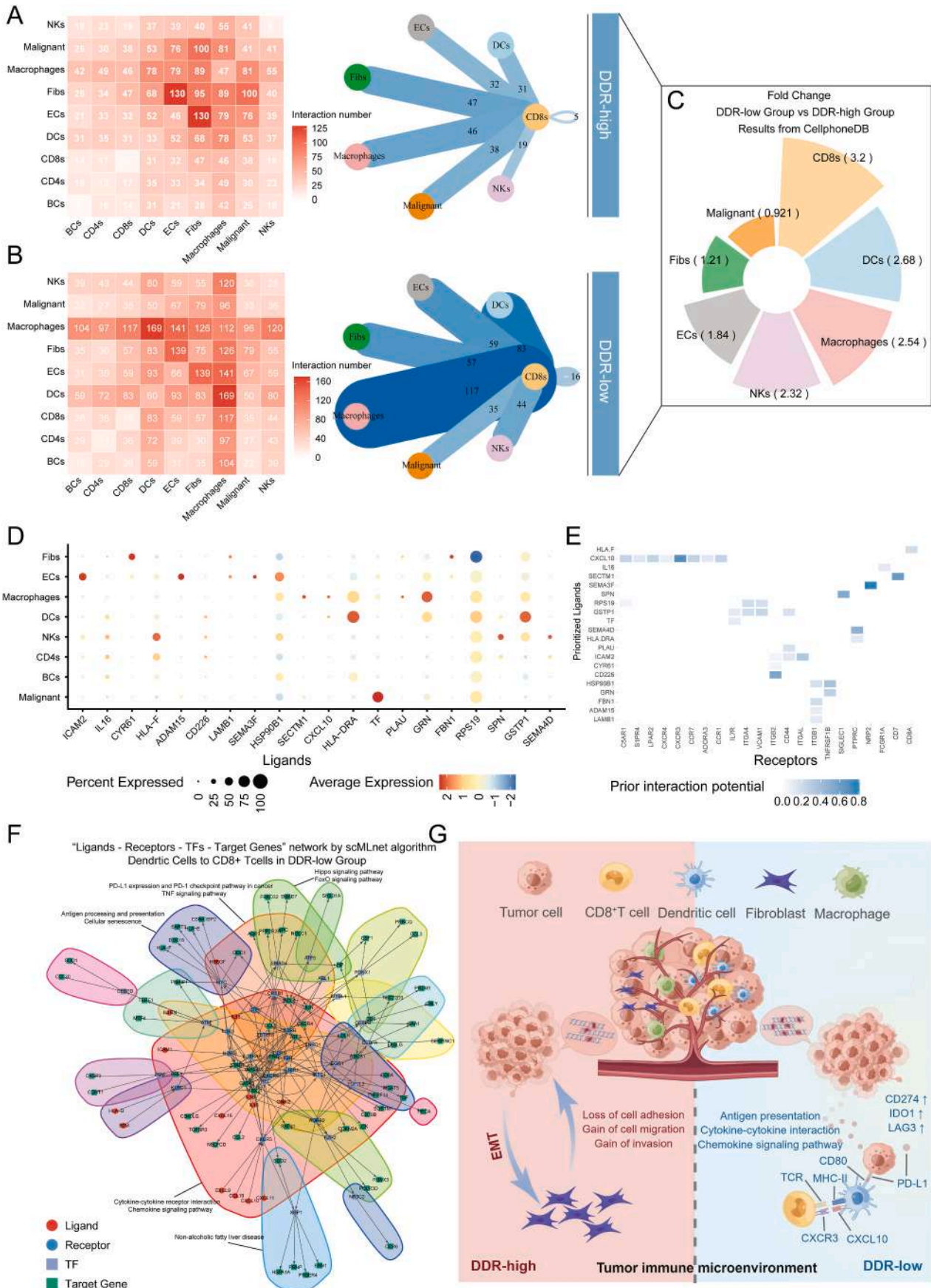
Fig. 3. Immune Therapy Blockade-Mediated Characteristics of the Immune Microenvironment by DDR. A. scRNA-seq of 34,708 filtered cells. The left panel shows cell annotation, and the right panel shows UMAP plots of cells under different treatment conditions and bar graphs of cell numbers under different clinical indices. B. Relative percentage of 10 cell populations in different treatment sources. C. Bar graphs of the numbers of malignant and non-malignant cells in different sample sources. D. UMAP plot (left panel) of 9966 malignant cells, with each color representing a corresponding sample source; a heat map (right panel) showing the staging features and treatment methods of different samples. E. UMAP plots (bottom panel) and cell proportion graphs (top panel) of the post-immune therapy HCC tumor microenvironment in different DDR score groups, with each color indicating the corresponding cell type. F. Volcano plot of the difference in gene expression between high and low DDR score groups in malignant cells. G. Bar graphs of significantly activated pathways in malignant cells in high and low DDR score groups (red and blue, respectively). H. Pseudo-temporal analysis of cell state transition from malignant to fibroblast-like state in high DDR score groups, with each cell colored by pseudo-time (top panel) and cell type (bottom panel), measuring the changes made to each cell through a process (e.g., differentiation). I. Heatmap of the relative expression of immune checkpoint molecules, immune activation molecules, and major histocompatibility complex molecules in different cell types in different DDR score groups, with data transformed by scaling.

and those in particular LAG-3 exhibited significantly elevated expression in CD8$^+$ T cells in the "DDR-low" patients (Fig. 3I). As for immunostimulatory molecules, tumor necrosis factor (TNF)-associated family signals were specifically enriched indicating that DDR impairment may induce successive tumor-killing (Fig. 3I, middle) and besides, T cell/B cell communication: CD27/CD70, T-cell/DC crosstalk via CD40LG/CD40 and CD80-86/CD28 were also observed, which showed generally up-regulated patterns in "DDR-high" group (Fig. 3I). Moreover, by measuring the MHC molecules, we showed that MHC I molecules HLA-A, B, C (classical) and HLA- E, F, G (non-classical) exhibited increasing partners and similarly cell type specific MHC II molecules (exclusively B cells, DCs and macrophages mediated) were simultaneously up-regulated in "DDR-low" patients (Fig. 3I). In summary, these phenomena indicated that DDR status characterized by DDRscore has certain regulatory roles in the TME to differentiate HCC patient receiving ICI

immunotherapy.

3.4. The CXCL10-CXCR3 axis induces DCs to cross-present antigen and recognize CD8$^+$ T cells under the low DDR state

Since cellular crosstalk was pronounced in HCC TME, we next employed multiple bioinformatic tools (CellPhoneDB, NicheNet, and scMLnet) to identify molecular interactions between ligand-receptor pairs within specific cell types under different DDR states in ICI treated patients. On a global scale, TME cell-cell communication underwent a dynamic reprogramming whereby "DDR-high" was centralized through fibroblast-endothelium axis whereas "DDR-high" had a complete shift towards macrophage-dominated pattern (Fig. 4A–B). Moreover, using CD8$^+$ T cells as recipient cells, we showed dynamic alterations of cellular crosstalk in response to changing DDR status

(caption on next page)

Fig. 4. Characteristics of cell communication mediated by different DDRs after immune therapy blockade. A-B. Heat maps (left panel) of ligand-receptor interactions between cell types from CellphoneDB, including malignant cells, stromal cells, and immune cells, and network graphs (right panel) represent the number of interactions between selected cell types and CD8$^+$ T cells, with dot colors representing cell types. A represents the group with high DDRscore, and B represents the group with a low DDRscore. C. Rose plots show the difference in cell interaction levels between groups with high and low DDRscore. D. Dot plots show the top 20 ligands with differential expression in the group with low DDRscores analyzed by NicheNet. The size of the dots represents the proportion of cells expressing the ligand. E. Heat maps show the receptor molecules interacting with the top 20 ligands in CD8$^+$ T cells. The color represents the potential of the interaction. F. Network graph of "ligand-receptor-transcription factor-target gene" interactions between dendritic cells and CD8$^+$ T cells in the group with low DDRscores. Different blocks represent the neighborhood structures extracted by iGraph network analysis data, with the text next to the blocks representing the corresponding biological pathways. Red circles represent ligands, blue circles represent receptors, purple blocks represent transcription factors, and green blocks represent target genes. G. This figure summarizes the different scRNA-seq immune ecosystems between HCCs with high and low DDRscores after immune therapy blockade. EMT, epithelial-mesenchymal transition; TCR, T cell receptor.

following ICI therapy. Those involved augmented communications with macrophages (fold-change FC = 2.68), DC (FC = 2.54) and NK cells (FC = 2.32) respectively in DDR-low group (Fig. 4B–C). Apart from communication arising from CD8$^+$ T cells self-interaction (though total number was low), interactions with endothelium, fibroblasts and tumor cells were less phenomenal (Fig. 4B–C). Looking at the ligand expression level, using NicheNet algorithm, we characterized the major ligand expression associated with varying DDR levels (Fig. 4D, Figs. S6A–B).

These results demonstrated that HLA-DRA and GSTP1 were highly expressed in DCs under "DDR-low" condition but down-regulated in "DDR-high" state. Macrophages, another highly regulated population, had up-regulated GRN in "DDR-low" group and HLA-DRA to a lesser extent in its expression was also significantly increased in "DDR-low" group (Fig. 4D, Figs. S6A–B). TF which binds to IL7R in CD8$^+$ T cells was the only highly-expressed ligand molecule significantly highly expressed in the "DDR-high" group (Fig. 4D, Figs. S6A–B). Since we have shown
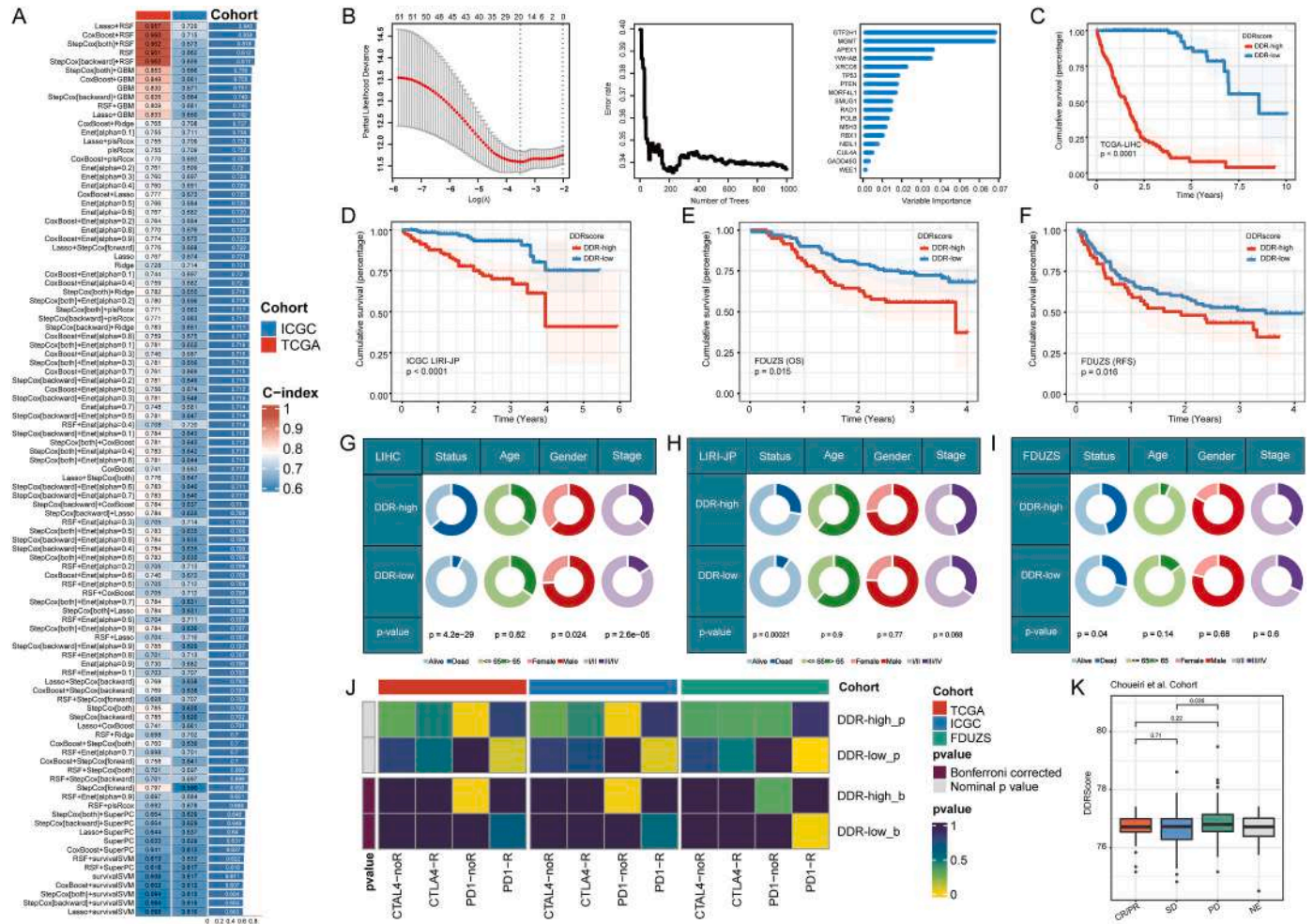

Fig. 5. A consensus DDRscore was developed and validated using a combination of bulk-seq data and machine learning methods. A. A total of 101 prediction models were calculated through a LOOCV framework, and the C-index was further calculated for each model on the training and validation datasets. B. The best λ was determined when the penalized likelihood deviation reached its minimum value in the TCGA-LIHC training cohort (left panel), the error rate in the random survival forest was used as the function of the classification tree (middle panel), and the out-of-bag importance values of the predicted genes were calculated (right panel). C-D. Kaplan-Meier OS curves of DDRscore in the TCGA-LIHC training cohort and the ICGC LIRI-JP validation cohort. E-F. Kaplan-Meier OS and RFS curves of DDRscore in the FDUZS cohort. G-I. Pie charts show the chi-squared test between DDRscore and clinical pathological factors in HCC samples from the TCGA-LIHC cohort, ICGC LIRI-JP cohort and FDUZS cohort. J. DDRscore grouping based on TIDE and Submap predictions for response to immune checkpoint inhibitors (PD-1 or CTLA4). K. Differences in DDRscore between different immune therapy efficacies were analyzed, and statistical differences between groups were tested using the Wilcoxon rank test. P < 0.05, **P < 0.01, ***P < 0.001.

CD8$^+$ T cells being a key interactor and potentially involved in multiple cellular cross-talks, we used CellphoneDB to further interrogate their potential interacting molecules particularly in "DDR-low" patients. We found that the central mediator of the DCs featuring high CXCL10 expression as previously identified in "DDR-low" patients had the highest co-expression with CXCR3, a CD8$^+$ T cell surface receptor (Fig. 4E). This "DCs-CD8$^+$ T cell" interaction axis was further investigated by generating a complete "ligand-receptor-transcription factor-target gene" network, and predicted a variety of immune-related pathways that could be regulated in "DDR-low" group. This interacting network not only confirmed previously discovered cross-talk via MHC presentation such as HLA-B, HLA-F/E and B2M but also oncogenic MYC gene activation potentially bridged via PD1/PD-L1 pathway (Fig. 4F). Interestingly, IFNG, a crucial target gene of the CXCL10-CXCR3 axis could be regulated via transcription factors including GATA3, REL, and TBX21 revealing a crucial role of CXCL10-CXCR3 axis in recruiting DCs and CD8$^+$ T cells to interact with and mediate the infiltration of CD8$^+$ T cells into tumor niche under a low DDR state (Fig. 4F, Table S3). To this end, our findings, supported by in-depth profiling using bioinformatic tools, depicted a dynamic alteration of the HCC TME characterized by DDR status following immunotherapy (Fig. 4G), probing into potential therapeutic strategies to be exploited in the future.

3.5. The DDR consensus signature predicts HCC prognosis and immunotherapy responsiveness

In order to further utilize the transcriptional signature developed from above, we extracted the 56 essential DDR genes identified through single cell RNA-seq and developed a machine learning-based integration technique to generate DDRscores using external bulk RNA-seq datasets. We utilized the LOOCV framework to fit 101 combinatory machine learning methods and applied the TCGA-LIHC cohort as the training dataset and and the ICGC-LIRI-JP cohort for validation. We calculated the C-index for each model (Fig. 5A). With that, we derived the best predictive model (Lasso + random survival forest, RSF) with an average C-index of 0.843, (Fig. 5A, right panel bars). The optimal λ was determined using the LOOCV framework when the partial likelihood deviation achieved its minimum (Fig. 5B, left panel). Under such a cutoff, RSF analysis with non-zero Lasso coefficients finally determined the importance of 17 DDR genes (Fig. 5B, right panel). The DDRscore for each patient was then determined using the regression coefficient weighted expression of 17 DDR genes in the RSF model. Upon demonstrating the robustness of the DDRscore model derived from 17-gene signature, we subsequently categorized patients into "DDR-high" or "DDR-low" group. Surprisingly, we found that the overall survival (OS) of the "DDR-high" patients was significantly lower than that of the "DDR-low" patients in both the TCGA-LIHC and the ICGC-LIRI-JP datasets (*P*-vaule <0.0001, Fig. 5C–D).

To further validate the DDRscore-stratified patient survival, we used RNA-seq data comprising 159 HCC patients with clinical prognostic record available in-house [46]. In accordance with the above conclusion, based on model developed on the selected 17 genes, the "DDR-low" group had improved outcomes for both OS and relapse free survival (RFS) as compared to the "DDR-low" group (OS *P*-value = 0.015, RFS *P*-value = 0.016, Fig. 5E–F). Further analysis using chi-square test also proved a survival benefit with "DDR-low" HCC patients across all three independent cohorts (p-vales<0.05) (Fig. 5G–I). Thus far, these results confirmed a robust model generated via quantitative DDR status estimation that might be a potential prognostic indicator to predict benefits in HCC patients.

Our data thus far pointed at an immune regulatory pattern through altered DDR status and since immune checkpoint inhibitors have been approved for first-line therapies in HCC, we utilized the TIDE algorithm to estimate the likely relationship between DDRscore and response to immunotherapy. The subclass mapping was also used to contrast the expression patterns of our established DDRscore groups with those of an

additional published dataset containing 47 immunotherapy-responsive melanoma patients [47]. Using TIDE algorithm model, all three independent cohorts showed a tendency of probable association between low DDRscore and PD-1 response whereas high DDRscore was inclined to PD-1 ineffectiveness (Fig. 5J, adjusted p-value showing in lighter colors). Finally, using an independent cohort, we found high DDRscore associated with disease progression (Fig. 5K, PD versus SD Wilcoxon p-value <0.05). Taken together, our results suggested extra values of DDRscore potentially linking with immunotherapy efficacy, a finding also proved by our the single-cell analysis from above.

3.6. Targeting HCC patients with high DDRscore via B-Raf pathway inhibition

In order to identify potential therapeutic targets linking with DDR status, especially those with high-DDR scores who may suffer from inferior clinical outcomes, we first calculated DDRscores across 22 HCC cell lines (Fig. 6A). We then retrieved reverse phase protein array (RPPA) data from the TCGA-LIHC cohort and correlated the DDRscore for individual patients with paired RPPA proteomic data. We found the B-Raf expression was positively correlated with DDRscore (Fig. 6B, Spearman's R2 > 0.3). Next, we applied CERES scores to assess the correlation between individual gene dependencies and DDRscore based on 22 liver cancer cell lines and this again filtered BRAF gene as an important predictor of high-DDR score (Spearman's R2 < −0.25), Fig. 6C). Since both analyses pointed at the BRAF gene as an important therapeutic target in HCC, we conducted RPPA targeted proteomics on an independent HCC sample set (11 pairs of HCC and adjacent normal tissues) to verify its druggability. Using a panel covering 384 key oncogenic and druggable proteins and their modified forms, we found the active form of B-Raf (phosphorylated B-Raf at serine 445) and its downstream target MARK3 and ERK1/2 were significantly elevated in HCC (p < 0.001, Fig. 6D–E). Meantime, we also found that BRAF was significantly upregulated in the DDR-high group (Fig. 6F). Together, these data, by incorporating external TCGA data and in-house RPPA profiling, untangled a potential therapeutic vulnerability by targeting B-Raf pathway in DDR-high patients that may be of clinically important for patient stratification.

4. Discussion

Understanding the relationship between DDR and TME regulation in HCC will provide valuable insights into the development targeted therapies through DNA repair related mechanisms. Previously, many studies either focused on gene knockout mouse models to investigate regulatory mechanisms or exploring genetic aberrations via mutation landscapes [48–50]. Pitifully, less is known about the crosstalk between DNA Damage Repair (DDR) and TME at single-cell resolution in HCC. We demonstrated that the DDR status of the malignant cells are heterogeneous in HCC and is largely associated with tumor stages. By developing the DDRscore using a selected subset of genes, we showed tumor cells with "high-DDR" scores bear upregulated PI3K and EGFR signaling pathway activity. This coincides with previously findings showing high PI3K pathway activity is a hallmark of chemotherapy resistance in patients across multiple cancer including HCC [51,52]. Conversely, malignant cells with low DDR trigger the TRAIL pathway activation, and this pathway (TRAIL-TRAIL-R system) has been shown to facilitate tumor cell death through various systemic functional disorder in a tumor environment-dependent manner partially supporting our data wherein dynamic alteration of TME was observed [53]. This reduced DDR activity of malignant cells may contribute to an anti-tumor response synergizing with the current clinical regimes of using PARP inhibitors or tumor radiotherapy. Based on the DDRscore classification, we identified NKs and B Cells (BCs) as being the major immune cell types dynamically altered between "DDR-high" and "DDR-low" patients. A sub-population of NKs (FCGR3A$^+$ NKs) was significantly elevated in the

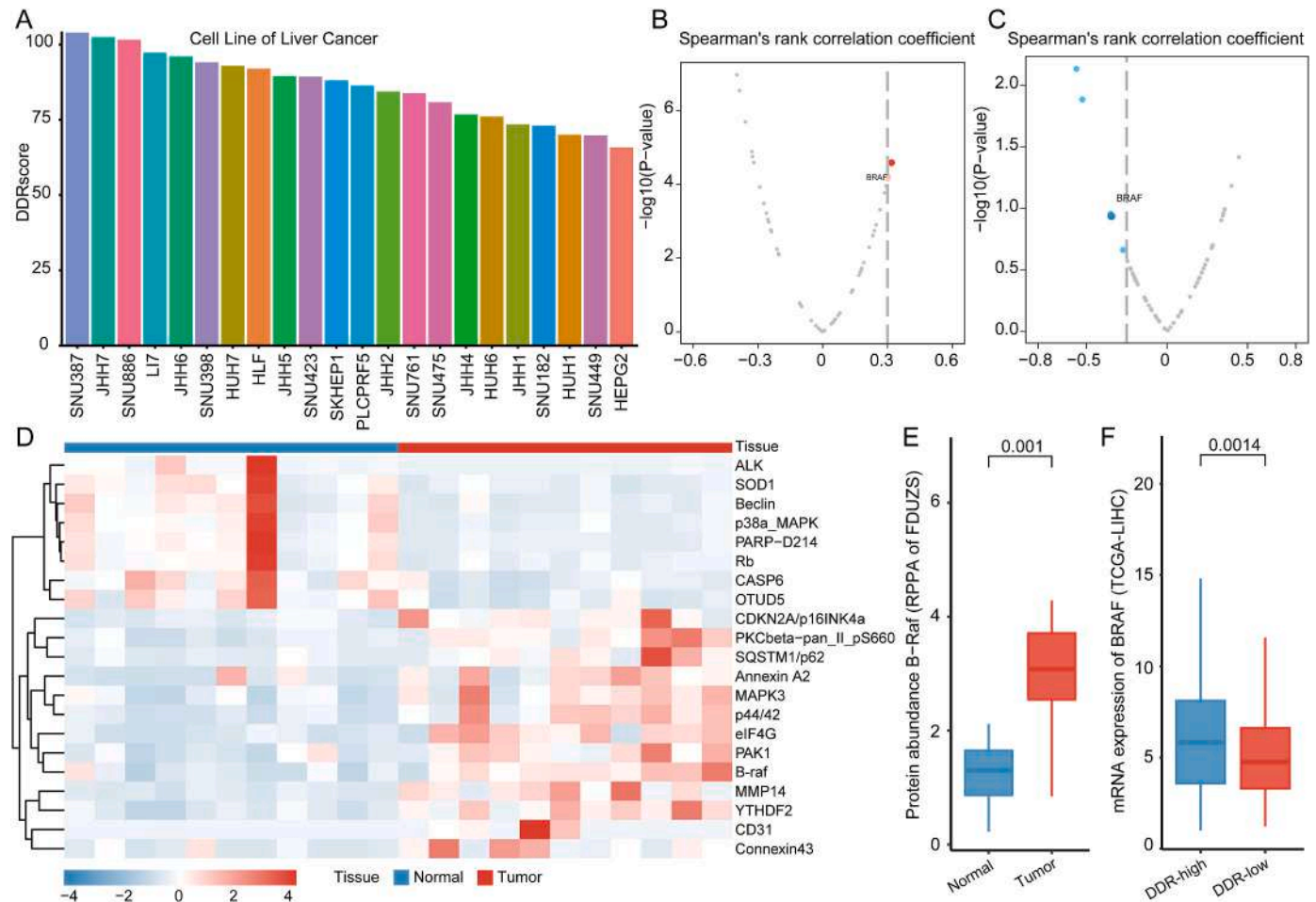**Fig. 6.** Identification of drug targets and high DDRscore groups with high drug sensitivity in HCC. A. DDRscore calculation of 22 liver cancer cell lines in CCLE based on a machine learning model. B. Spearman correlation and significance between the DDRscore and protein expression levels of drug targets, represented in a volcano plot. Red dots indicate a positive correlation. C. Spearman correlation and significance between the DDRscore and CERES scores of drug targets, represented in a volcano plot. Blue dots indicate a significant negative correlation. Common targets are marked in the volcano plot. D. Heatmap shows the protein expression levels of 21 significantly different drug targets in HCC and normal tissues. E. Difference in protein expression of BRAF between HCC and normal tissues. F. Difference in mRNA expression of BRAF between DDR-high and DDR-low group in TCGA-LIHC cohort.

low DDR group and was potentially involved in antigen processing and MHC class I-mediated presentation. Meanwhile, CD20$^+$ BCs as being present in "DDR-high" patients have activated cGAS-STING pathway. Similarly. previous studies have shown that STING activation induces IL-35 secretion by BCs causing reduction the number of NKs, thereby suppressing the anti-tumor response [54]. In contrast, GSTA1$^+$ NK subpopulation was significantly increased with high DDR levels revealing the existence of potential heterogeneity within a cell subset. Simultaneously, BCs also feature PPAR activation under DRR high condition suggesting a probably connection whereby PPAR signaling maintains the dynamic balance of liver lipid metabolism by participating in a variety of biological processes such as fatty acid oxidation, which involves GSTA1 during inflammatory response [55–57]. These together confirms the existing interplay between NKs and BCs during the oncogenic shift dictated by DDR status, a mechanism, by creating an immunosuppressive microenvironment through the lipid metabolism reprogramming in DDR-high patients, potentially impacts on efficacy of immunotherapies in HCC.

Since immunotherapy in HCC remains dismal, several studies have revealed that tumor heterogeneity significantly affects the efficiency of immunotherapies, particularly ICIs [58]. Our follow-up study on immunotherapy-treated HCC patients demonstrated that DDR-directed malignant cell alteration being present in different patterns in the cellular ecosystem of HCC. In particular, at the single cell level, distinct

DDR status exhibit dynamically altered infiltration of DCs and CD8$^+$ T cells. Of the malignant cells, "high DDR" is characterized by activation of the EMT pathway, decreased adhesion of malignant epithelium, and the occurrence of invasion and metastasis. Recent research demonstrates that stimulation and activation of the EMT process can enhance homologous recombination-dependent DNA repair and tumor radiation resistance, a finding supporting our discovery [59]. In contrast, low DDR is characterized by a decreased propagation of malignant cells, which is companied by boosting of DCs and CD8$^+$ T cells with increased expression of the PD-1, IDO1, LAG3, and MHC-related genes. In agreement with this, attenuation of DDR activation via STING/IRF3 has been shown to lead to elevated DCs [60]. In addition, implementation of Olaparib (PARP inhibitor) to generate a low DDR environment also results in the upregulation of CD80, CD86, and MHC II expression levels and increased IFN-γ and TNF-α production in CD8$^+$ T cells, further supporting our hypothesis [61]. In summary, our data, supported by previous findings, depict a low DDR TME defined by antigen cross-presentation via DCs and CD8$^+$ T cells to affect tumor antigenicity. More importantly, radiotherapy has been shown to facilitate DNA damage in tumors by synergistically recruiting DCs and CD8$^+$ T cells [62]. Therefore, we propose that for HCC patients with low DDR, who are primed to sensitize with immunotherapy may benefit from concurrent radiotherapy. For HCC with a high level of DDR, radiotherapy has the potential to reduce DDR efficacy in the first place, thereby increasing

tumor antigenicity by TME reprogramming and predisposing to ICI therapy.

By constructing a "ligands-receptors-transcription factors-target genes" network for HCC in low DDR patients, we identified the CXCL10-CXCR3 axis as a critical driver for the interactions between DCs and CD8$^+$ T cells. CXCL10 is a critical chemokine for effector T cell infiltration into the tumor microenvironment and immunotherapy effectiveness and targeting CXCL10 may have significant anti-tumor potential [63]. Furthermore, the production of type I interferon, tumor necrosis factor-α (TNF-α), and subsequent CXCL10 has been shown to be induced by activation of innate immune pathways involved in pathogen response, such as the cytosolic nucleic acid sensor cGAS-STING pathway linking DDR with immune regulation [64]. In addition, existing evidence suggests that CXCL10 can enhance the efficacy of ICIs in the treatment of homologous recombination-deficient tumors [65], and the combination treatment of CXCL10 oncolytic adenovirus and PD-1 antibody can increase the recruitment of CXCR3$^+$ T cells in the TME to enhance the efficacy of ICIs [65,66]. CXCR3 expression in peripheral T cells can be used as a biomarker to predict the efficacy of PD-1 antibodies, and ectopic induction of intratumorally CXCL9/10 can help PD-1 antibodies further inhibit tumor growth by increasing the proportion of CXCR3$^+$ T cells in the TME [67]. In addition, our analysis uncovers IFNG as being an essential target of the CXCL10-CXCR3 axis and this can be regulated by transcription factors GATA3, REL, and TBX21. Together, those data provide ample amount of evidence uncovering a potentially novel mechanism of CXCL10-CXCR3 mediated immune regulation in DDR-low HCC patients.

To further validate our findings concluded from our single cell analysis, we then developed an integration pipeline to construct a consensus DDRscore based on bulk-seq data. Using external bulk RNA-seq datasets. We built a machine learning model through the LOOCV framework. The advantage of the comprehensive procedure is that it can fit a model with consistent performance on the prognosis of HCC based on a variety of machine learning algorithms and their combinations, which can further reduce the dimensionality of variables. Intriguingly, the resultant 17-DDR gene signature has been shown as a decisive indicator to predict the overall survival (OS) in HCC patients. The performance was tested against both external and in-house dataset using retrospectively corrected samples assuring the robustness of the DDRscore under various experimental settings. This DDRscore may also have added values of predicting resistance to anti-PD-1 therapy in HCC though further clinical experimental designs need in place. More importantly, based on this DDRscore system, we identified the corresponding druggable targets via RPPA proteomic profiles making it more attractive for clinical translation and implementation. Several studies have demonstrated that BRAF may influence the response of HCC to anti-cancer drugs [68,69]. Additionally, BRAF may also be a predictive biomarker for reduced response to sorafenib in HCC [70]. Therefore. the identified BRAF at both transcript and protein levels as a potential therapeutic target may be of proven clinical significance in directing HCC patient stratification who bear high DDRscores. However, further evidence is required to elucidate the mechanisms to allow future clinical experimental deign.

On conducting these serial experiments using external database and in-house multi-omics experiments, we characterize a DDR-based gene signature systematically shedding light on the role of DNA repair mechanisms in HCC progression and treatment-related efficacy. These findings highlight the importance of DDR-induced TME alteration in primary and immunotherapy-treated HCC. The DDRscore developed may facilitate future implementation of personalized therapies including inhibition of ICIs and BRAF adhering to current clinical practice. In the future, by incorporating novel approaches from both single cell and spatial multi-omics perspectives, novel clinical concepts may be translated into advancement of precision medicine in HCC.

Ethical approval and consent to participate

This study was approved by the Institutional Review Board of the Zhongshan Hospital, Fudan University (B2022-048 R). The study was performed in accordance with the Helsinki Declaration and Rules of Good Clinical Practice. All participants signed written informed consents after fully explained.

Consent for publication

We have obtained written informed consent from the patient and the written consent is in the patient's hospital record.

Data and code availability

The method section describes all the data utilized for analysis and processing in this study. On reasonable request, the corresponding author will provide the data and code supporting the conclusions of this work.

CRediT authorship contribution statement

Weifeng Hong: Writing – original draft, Visualization, Validation, Methodology, Formal analysis, Data curation, Conceptualization. **Yang Zhang:** Resources, Methodology, Investigation, Formal analysis, Data curation. **Siwei Wang:** Software, Methodology, Investigation, Formal analysis, Data curation. **Danxue Zheng:** Software, Resources, Project administration, Methodology. **Shujung Hsu:** Resources, Methodology, Investigation. **Jian Zhou:** Writing – review & editing, Supervision. **Jia Fan:** Writing – review & editing, Supervision. **Zhaochong Zeng:** Writing – review & editing, Supervision. **Nan Wang:** Validation, Software. **Zhiyong Ding:** Validation, Software. **Min Yu:** Writing – review & editing, Supervision, Software, Project administration, Methodology, Conceptualization. **Qiang Gao:** Writing – review & editing, Validation, Supervision, Project administration, Data curation, Conceptualization. **Shisuo Du:** Writing – review & editing, Supervision, Software, Resources, Funding acquisition, Conceptualization.

Declaration of competing interest

NW and ZYD are full-time employees of Fynn Biotechnologies. Other authors declare no competing interests.

Acknowledgement

Abbreviations

DDR	DNA damage repair
HCC	hepatocellular carcinoma
RPPA	reverse phase protein array
DR	damage reversal
BER	base excision repair
NER	nucleotide excision repair

MMR	mismatch repair
SSB	single-strand break
DSB	double-strand break
HR	homologous recombination
NHEJ	non-homologous end joining
PFS	progression-free survival
TME	tumor microenvironment
NAL:	neoantigen load
TILs	tumor-infiltrating lymphocytes
FDA	Food and Drug Administration
scRNA-seq	Single-cell RNA sequencing
ICB	immune checkpoint blockade
AJCC	American Joint Committee on Cancer
bulk-seq	bulk sequencing
UMAP	unified manifold approximation and projection
hdWGCNA	high-dimensional weighted gene co-expression network analysis
EGFR	epidermal growth factor receptor
PI3Ks	phosphatidylinositol 3-kinases
TRAIL:	tumor necrosis factor-related apoptosis-inducing ligand
OR	odds ratio
OS	overall survival
PD	progressive disease
SD	stable disease
ICIs	immune checkpoint inhibitors
TNF-α:	tumor necrosis factor-α
NKs	natural killer cells
DCs	dendritic cells
ECs	endothelial cells

Appendix A. Supplementary data

Supplementary data to this article can be found online at https://doi.org/10.1016/j.canlet.2023.216594.

References

[1] D. Hanahan, Hallmarks of cancer: new dimensions, Cancer Discov. 12 (2022) 31–46.

[2] C. Huang, S. Zhou, C. Zhang, Y. Jin, G. Xu, L. Zhou, G. Ding, T. Pang, S. Jia, L. Cao, ZC3H13-mediated N6-methyladenosine modification of PHF10 is impaired by fisetin which inhibits the DNA damage response in pancreatic cancer, Cancer Lett. 530 (2022) 16–28.

[3] C.A. Kunos, S.J. Andrews, K.N. Moore, H.S. Chon, S.P. Ivy, Randomized phase II trial of triapine-cisplatin-radiotherapy for locally advanced stage uterine cervix or vaginal cancers, Front. Oncol. 9 (2019) 1067.

[4] D.T. Le, J.N. Uram, H. Wang, B.R. Bartlett, H. Kemberling, A.D. Eyring, A.D. Skora, B.S. Luber, N.S. Azad, D. Laheru, B. Biedrzycki, R.C. Donehower, A. Zaheer, G. A. Fisher, T.S. Crocenzi, J.J. Lee, S.M. Duffy, R.M. Goldberg, A. de la Chapelle, M. Koshiji, F. Bhaijee, T. Huebner, R.H. Hruban, L.D. Wood, N. Cuka, D.M. Pardoll, N. Papadopoulos, K.W. Kinzler, S. Zhou, T.C. Cornish, J.M. Taube, R.A. Anders, J. R. Eshleman, B. Vogelstein, L.A. Diaz Jr., PD-1 blockade in tumors with mismatch-repair deficiency, N. Engl. J. Med. 372 (2015) 2509–2520.

[5] W. Yan, J. Qiu, M. Yang, A. Xu, M. Ma, Q. Yuan, X. Ma, W. Liang, X. Li, Y. Lu, CXCL10 mediates CD8(+) T cells to facilitate vessel normalization and improve the efficacy of cetuximab combined with PD-1 checkpoint inhibitors in colorectal cancer, Cancer Lett. 567 (2023), 216263.

[6] R.M. Chabanon, J.C. Soria, C.J. Lord, S. Postel-Vinay, Beyond DNA repair: the novel immunological potential of PARP inhibitors, Mol Cell Oncol 6 (2019), 1585170.

[7] C. Zhu, Y. Xie, Q. Li, Z. Zhang, J. Chen, K. Zhang, X. Xia, D. Yu, D. Chen, Z. Yu, J. Chen, CPSF6-mediated XBP1 3'UTR shortening attenuates cisplatin-induced ER stress and elevates chemo-resistance in lung adenocarcinoma, Drug Resist. Updates : reviews and commentaries in antimicrobial and anticancer chemotherapy 68 (2023), 100933.

[8] B. Farhood, E. Khodamoradi, M. Hoseini-Ghahfarokhi, E. Motevaseli, H. Mirtavoos-Mahyari, A. Eleojo Musa, M. Najafi, TGF-β in radiotherapy: mechanisms of tumor resistance and normal tissues injury, Pharmacol. Res. 155 (2020), 104745.

[9] S. Upadhaya, S.T. Neftelino, J.P. Hodge, C. Oliva, J.R. Campbell, J.X. Yu, Combinations take centre stage in PD1/PDL1 inhibitor clinical trials, Nat. Rev. Drug Discov. 20 (2021) 168–169.

[10] T. Sen, B.L. Rodriguez, L. Chen, C.M.D. Corte, N. Morikawa, J. Fujimoto, S. Cristea, T. Nguyen, L. Diao, L. Li, Y. Fan, Y. Yang, J. Wang, B.S. Glisson, Wistuba II, J. Sage, J.V. Heymach, D.L. Gibbons, L.A. Byers, Targeting DNA damage response promotes antitumor immunity through STING-mediated T-cell activation in small cell lung cancer, Cancer Discov. 9 (2019) 646–661.

[11] K.W. Mouw, M.S. Goldberg, P.A. Konstantinopoulos, A.D. D'Andrea, DNA damage and repair biomarkers of immunotherapy response, Cancer Discov. 7 (2017) 675–693.

[12] w.b.e. Cancer Genome Atlas Research Network, Electronic address, N. Cancer genome atlas research, comprehensive and integrative genomic characterization of hepatocellular carcinoma, Cell 169 (2017) 1327–1341, e1323.

[13] M. Duan, J. Hao, S. Cui, D.L. Worthley, S. Zhang, Z. Wang, J. Shi, L. Liu, X. Wang, A. Ke, Y. Cao, R. Xi, X. Zhang, J. Zhou, J. Fan, C. Li, Q. Gao, Diverse modes of clonal evolution in HBV-related hepatocellular carcinoma revealed by single-cell genome sequencing, Cell Res. 28 (2018) 359–373.

[14] Z. Wang, J. Zhao, G. Wang, F. Zhang, Z. Zhang, F. Zhang, Y. Zhang, H. Dong, X. Zhao, J. Duan, H. Bai, Y. Tian, R. Wan, M. Han, Y. Cao, L. Xiong, L. Liu, S. Wang, S. Cai, T.S.K. Mok, J. Wang, Comutations in DNA damage response pathways serve as potential biomarkers for immune checkpoint blockade, Cancer Res. 78 (2018) 6486–6496.

[15] X. Cui, L. Han, L. Cui, G. Fu, E. Liu, D. Wang, B. Song, Y. Zhang, W. Zhou, H. Wang, J. Fu, Immune index: a gene and cell prognostic signature for immunotherapy response prediction in hepatocellular carcinoma, Pharmacol. Res. 187 (2023), 106583.

[16] Y.S. Ma, T. Huang, X.M. Zhong, H.W. Zhang, X.L. Cong, H. Xu, G.X. Lu, F. Yu, S. B. Xue, Z.W. Lv, D. Fu, Proteogenomic characterization and comprehensive integrative genomic analysis of human colorectal cancer liver metastasis, Mol. Cancer 17 (2018) 139.

[17] T.W. Chen, W.Z. Hung, S.F. Chiang, W.T. Chen, T.W. Ke, J.A. Liang, C.Y. Huang, P. C. Yang, K.C. Huang, K.S.C. Chao, Dual inhibition of TGFβ signaling and CSF1/CSF1R reprograms tumor-infiltrating macrophages and improves response to chemotherapy via suppressing PD-L1, Cancer Lett. 543 (2022), 215795.

[18] R.S. Finn, S. Qin, M. Ikeda, P.R. Galle, M. Ducreux, T.Y. Kim, M. Kudo, V. Breder, P. Merle, A.O. Kaseb, D. Li, W. Verret, D.Z. Xu, S. Hernandez, J. Liu, C. Huang, S. Mulla, Y. Wang, H.Y. Lim, A.X. Zhu, A.L. Cheng, I.M. Investigators, Atezolizumab plus bevacizumab in unresectable hepatocellular carcinoma, N. Engl. J. Med. 382 (2020) 1894–1905.

[19] Y. Lu, A. Yang, C. Quan, Y. Pan, H. Zhang, Y. Li, C. Gao, H. Lu, X. Wang, P. Cao, H. Chen, S. Lu, G. Zhou, A single-cell atlas of the multicellular ecosystem of primary and metastatic hepatocellular carcinoma, Nat. Commun. 13 (2022) 4594.

[20] L. Ma, S. Heinrich, L. Wang, F.L. Keggenhoff, S. Khatib, M. Forgues, M. Kelly, S. M. Hewitt, A. Saif, J.M. Hernandez, D. Mabry, R. Kloeckner, T.F. Greten, J. Chaisaingmongkol, M. Ruchirawat, J.U. Marquardt, X.W. Wang, Multiregional single-cell dissection of tumor and immune cells reveals stable lock-and-key features in liver cancer, Nat. Commun. 13 (2022) 7533.

[21] D.A. Braun, Y. Hou, Z. Bakouny, M. Ficial, M. Sant' Angelo, J. Forman, P. Ross-Macdonald, A.C. Berger, O.A. Jegede, L. Elagina, J. Steinharter, M. Sun, M. Wind-Rotolo, J.C. Pignon, A.D. Cherniack, L. Lichtenstein, D. Neuberg, P. Catalano, G. J. Freeman, A.H. Sharpe, D.F. McDermott, E.M. Van Allen, S. Signoretti, C.J. Wu, S. A. Shukla, T.K. Choueiri, Interplay of somatic alterations and immune infiltration modulates response to PD-1 blockade in advanced clear cell renal cell carcinoma, Nat. Med. 26 (2020) 909–918.

[22] R. Gao, S. Bai, Y.C. Henderson, Y. Lin, A. Schalck, Y. Yan, T. Kumar, M. Hu, E. Sei, A. Davis, F. Wang, S.F. Shaitelman, J.R. Wang, K. Chen, S. Moulder, S.Y. Lai, N. E. Navin, Delineating copy number and clonal substructure in human tumors from single-cell transcriptomes, Nat. Biotechnol. 39 (2021) 599–608.

[23] T. Stuart, A. Butler, P. Hoffman, C. Hafemeister, E. Papalexi, W.M. Mauck, Y. Hao, M. Stoeckius, P. Smibert, R. Satija, Comprehensive integration of single-cell data, Cell 177 (2019).

[24] L. Zappia, B. Phipson, A. Oshlack, Exploring the single-cell RNA-seq analysis landscape with the scRNA-tools database, PLoS Comput. Biol. 14 (2018), e1006245.

[25] S. Morabito, E. Miyoshi, N. Michael, S. Shahin, A.C. Martini, E. Head, J. Silva, K. Leavy, M. Perez-Rosendahl, V. Swarup, Single-nucleus chromatin accessibility and transcriptomic characterization of Alzheimer's disease, Nat. Genet. 53 (2021) 1143–1155.

[26] L. He, Y. Fan, Y. Zhang, T. Tu, Q. Zhang, F. Yuan, C. Cheng, Single-cell transcriptomic analysis reveals circadian rhythm disruption associated with poor prognosis and drug-resistance in lung adenocarcinoma, J. Pineal Res. 73 (2022), e12803.

[27] L. Jerby-Arnon, P. Shah, M.S. Cuoco, C. Rodman, M.J. Su, J.C. Melms, R. Leeson, A. Kanodia, S. Mei, J.R. Lin, S. Wang, B. Rabasha, D. Liu, G. Zhang, C. Margolais, O. Ashenberg, P.A. Ott, E.I. Buchbinder, R. Haq, F.S. Hodi, G.M. Boland, R. J. Sullivan, D.T. Frederick, B. Miao, T. Moll, K.T. Flaherty, M. Herlyn, R. W. Jenkins, R. Thummalapalli, M.S. Kowalczyk, I. Canadas, B. Schilling, A.N. R. Cartwright, A.M. Luoma, S. Malu, P. Hwu, C. Bernatchez, M.A. Forget, D. A. Barbie, A.K. Shalek, I. Tirosh, P.K. Sorger, K. Wucherpfennig, E.M. Van Allen, D. Schadendorf, B.E. Johnson, A. Rotem, O. Rozenblatt-Rosen, L.A. Garraway, C. H. Yoon, B. Izar, A. Regev, A cancer cell program promotes T cell exclusion and resistance to checkpoint blockade, Cell 175 (2018) 984–997, e924.

[28] L. Zheng, S. Qin, W. Si, A. Wang, B. Xing, R. Gao, X. Ren, L. Wang, X. Wu, J. Zhang, N. Wu, N. Zhang, H. Zheng, H. Ouyang, K. Chen, Z. Bu, X. Hu, J. Ji, Z. Zhang, Pan-cancer single-cell landscape of tumor-infiltrating T cells, Science 374 (2021) abe6474.

[29] M. Schubert, B. Klinger, M. Klunemann, A. Sieber, F. Uhlitz, S. Sauer, M.J. Garnett, N. Bluthgen, J. Saez-Rodriguez, Perturbation-response genes reveal signaling footprints in cancer gene expression, Nat. Commun. 9 (2018) 20.

[30] Z. Gu, Complex heatmap visualization 1 (2022) e43.

[31] T. Wu, E. Hu, S. Xu, M. Chen, P. Guo, Z. Dai, T. Feng, L. Zhou, W. Tang, L. Zhan, X. Fu, S. Liu, X. Bo, G. Yu, clusterProfiler 4.0: a universal enrichment tool for interpreting omics data, Innovation 2 (2021), 100141.

[32] X. Qiu, Q. Mao, Y. Tang, L. Wang, R. Chawla, H.A. Pliner, C. Trapnell, Reversed graph embedding resolves complex single-cell trajectories, Nat. Methods 14 (2017) 979–982.

[33] R. Vento-Tormo, M. Efremova, R.A. Botting, M.Y. Turco, M. Vento-Tormo, K. B. Meyer, J.E. Park, E. Stephenson, K. Polanski, A. Goncalves, L. Gardner, S. Holmqvist, J. Henriksson, A. Zou, A.M. Sharkey, B. Millar, B. Innes, L. Wood, A. Wilbrey-Clark, R.P. Payne, M.A. Ivarsson, S. Lisgo, A. Filby, D.H. Rowitch, J. N. Bulmer, G.J. Wright, M.J.T. Stubbington, M. Haniffa, A. Moffett, S. A. Teichmann, Single-cell reconstruction of the early maternal-fetal interface in humans, Nature 563 (2018) 347–353.

[34] J. Cheng, J. Zhang, Z. Wu, X. Sun, Inferring microenvironmental regulation of gene expression from single-cell RNA sequencing data using scMLnet with an application to COVID-19, Briefings Bioinf. 22 (2021) 988–1005.

[35] Z. Liu, L. Liu, S. Weng, C. Guo, Q. Dang, H. Xu, L. Wang, T. Lu, Y. Zhang, Z. Sun, X. Han, Machine learning-based integration develops an immune-derived lncRNA signature for improving outcomes in colorectal cancer, Nat. Commun. 13 (2022) 816.

[36] I. Todd, O.H. Negm, J. Reps, P. Radford, G. Figueredo, E.M. McDermott, E. Drewe, R.J. Powell, S. Bainbridge, M. Hamed, S. Crouch, J. Garibaldi, S. St-Gallay, L. C. Fairclough, P.J. Tighe, A signalome screening approach in the autoinflammatory disease TNF receptor associated periodic syndrome (TRAPS) highlights the anti-inflammatory properties of drugs for repurposing, Pharmacol. Res. 125 (2017) 188–200.

[37] C. Yang, X. Huang, Y. Li, J. Chen, Y. Lv, S. Dai, Prognosis and personalized treatment prediction in TP53-mutant hepatocellular carcinoma: an in silico strategy towards precision oncology, Briefings Bioinf. 22 (2021).

[38] R.M. Meyers, J.G. Bryan, J.M. McFarland, B.A. Weir, A.E. Sizemore, H. Xu, N. V. Dharia, P.G. Montgomery, G.S. Cowley, S. Pantel, A. Goodale, Y. Lee, L.D. Ali, G. Jiang, R. Lubonja, W.F. Harrington, M. Strickland, T. Wu, D.C. Hawes, V. A. Zhivich, M.R. Wyatt, Z. Kalani, J.J. Chang, M. Okamoto, K. Stegmaier, T. R. Golub, J.S. Boehm, F. Vazquez, D.E. Root, W.C. Hahn, A. Tsherniak, Computational correction of copy number effect improves specificity of CRISPR-Cas9 essentiality screens in cancer cells, Nat. Genet. 49 (2017) 1779–1784.

[39] C. Cancer, Cell Line Encyclopedia, C. Genomics of Drug Sensitivity in Cancer, Pharmacogenomic agreement between two cancer cell line data sets, Nature 528 (2015) 84–87.

[40] P. Geeleher, Z. Zhang, F. Wang, R.F. Gruener, A. Nath, G. Morrison, S. Bhutra, R. L. Grossman, R.S. Huang, Discovering novel pharmacogenomic biomarkers by imputing drug response in cancer patients from large genomics studies, Genome Res. 27 (2017) 1743–1751.

[41] Y.W. Yi, K.S. You, J.S. Park, S.G. Lee, Y.S. Seong, Ribosomal protein S6: a potential therapeutic target against cancer? Int. J. Mol. Sci. 23 (2021).

[42] K.A. Hoadley, C. Yau, T. Hinoue, D.M. Wolf, A.J. Lazar, E. Drill, R. Shen, A. M. Taylor, A.D. Cherniack, V. Thorsson, R. Akbani, R. Bowlby, C.K. Wong, M. Wiznerowicz, F. Sanchez-Vega, A.G. Robertson, B.G. Schneider, M.S. Lawrence, H. Noushmehr, T.M. Malta, N. Cancer Genome Atlas, J.M. Stuart, C.C. Benz, P. W. Laird, Cell-of-Origin patterns dominate the molecular classification of 10,000 tumors from 33 types of cancer, Cell 173 (2018) 291–304, e296.

[43] P.G. Pilie, C. Tang, G.B. Mills, T.A. Yap, State-of-the-art strategies for targeting the DNA damage response in cancer, Nat. Rev. Clin. Oncol. 16 (2019) 81–104.

[44] B. Cheng, Y. Wang, A.A. Ayanlaja, J. Zhu, P.A. Kambey, Z. Qiu, C. Zhang, W. Hu, Glutathione S-transferases S1, Z1 and A1 serve as prognostic factors in glioblastoma and promote drug resistance through antioxidant pathways, Cells (2022) 11.

[45] S. Edin, T. Kaprio, J. Hagstrom, P. Larsson, H. Mustonen, C. Bockelman, K. Strigard, U. Gunnarsson, C. Haglund, R. Palmqvist, The prognostic importance of CD20(+) B lymphocytes in colorectal cancer and the relation to other immune cell subsets, Sci. Rep. 9 (2019), 19997.

[46] Q. Gao, H. Zhu, L. Dong, W. Shi, R. Chen, Z. Song, C. Huang, J. Li, X. Dong, Y. Zhou, Q. Liu, L. Ma, X. Wang, J. Zhou, Y. Liu, E. Boja, A.I. Robles, W. Ma, P. Wang, Y. Li, L. Ding, B. Wen, B. Zhang, H. Rodriguez, D. Gao, H. Zhou, J. Fan, Integrated proteogenomic characterization of HBV-related hepatocellular carcinoma, Cell 179 (2019) 561–577, e522.

[47] W. Roh, P.L. Chen, A. Reuben, C.N. Spencer, P.A. Prieto, J.P. Miller, V. Gopalakrishnan, F. Wang, Z.A. Cooper, S.M. Reddy, C. Gumbs, L. Little, Q. Chang, W.S. Chen, K. Wani, M.P. De Macedo, E. Chen, J.L. Austin-Breneman, H. Jiang, J. Roszik, M.T. Tetzlaff, M.A. Davies, J.E. Gershenwald, H. Tawbi, A. J. Lazar, P. Hwu, W.J. Hwu, A. Diab, I.C. Glitza, S.P. Patel, S.E. Woodman, R. N. Amaria, V.G. Prieto, J. Hu, P. Sharma, J.P. Allison, L. Chin, J. Zhang, J. A. Wargo, P.A. Futreal, Integrated molecular analysis of tumor biopsies on sequential CTLA-4 and PD-1 blockade reveals markers of response and resistance, Sci. Transl. Med. 9 (2017).

[48] J. Lin, J. Shi, H. Guo, X. Yang, Y. Jiang, J. Long, Y. Bai, D. Wang, X. Yang, X. Wan, L. Zhang, J. Pan, K. Hu, M. Guan, L. Huo, X. Sang, K. Wang, H. Zhao, Alterations in DNA damage repair genes in primary liver cancer, Clin. Cancer Res. 25 (2019) 4701–4711.

[49] C. Wang, H. Tang, A. Geng, B. Dai, H. Zhang, X. Sun, Y. Chen, Z. Qiao, H. Zhu, J. Yang, J. Chen, Q. He, N. Qin, J. Xie, R. Tan, X. Wan, S. Gao, Y. Jiang, F.L. Sun,

[50] Z. Mao, Rational combination therapy for hepatocellular carcinoma with PARP1 and DNA-PK inhibitors, Proc. Natl. Acad. Sci. U. S. A. 117 (2020) 26356–26365.

[51] S. Ma, J. Zhang, Q. Guo, C. Cao, K. Bao, L. Liu, C.D. Chen, Z. Liu, J. Yang, N. Yang, Z. Yao, L. Shi, Disrupting PHF8-TOPBP1 connection elicits a breast tumor-specific vulnerability to chemotherapeutics, Cancer Lett. 530 (2022) 29–44.

[52] W. Blum, B. Schwaller, Calretinin is essential for mesothelioma cell growth/survival in vitro: a potential new target for malignant mesothelioma therapy? Int. J. Cancer 133 (2013) 2077–2088.

[53] M.D.A. Paskeh, F. Ghadyani, M. Hashemi, A. Abbaspour, A. Zabolian, S. Javanshir, M. Razzazan, S. Mirzaei, M. Entezari, M.A.S.B. Goharrizi, S. Salimimoghadam, A. R. Aref, A. Kalbasi, R. Rajabi, M. Rashidi, A. Taheriazam, G. Sethi, Biological impact and therapeutic perspective of targeting PI3K/Akt signaling in hepatocellular carcinoma: promises and Challenges, Pharmacol. Res. 187 (2023), 106553.

[54] S. von Karstedt, A. Montinaro, H. Walczak, Exploring the TRAILs less travelled: TRAIL in cancer biology and therapy, Nat. Rev. Cancer 17 (2017) 352–366.

[55] S. Li, B. Mirlekar, B.M. Johnson, W.J. Brickey, J.A. Wrobel, N. Yang, D. Song, S. Entwistle, X. Tan, M. Deng, Y. Cui, W. Li, B.G. Vincent, M. Gale Jr., Y. Pylayeva-Gupta, J.P. Ting, STING-induced regulatory B cells compromise NK function in cancer immunity, Nature 610 (2022) 373–380.

[56] A. Christofides, E. Konstantinidou, C. Jani, V.A. Boussiotis, The role of peroxisome proliferator-activated receptors (PPAR) in immune responses, Metabolism 114 (2021), 154338.

[57] Y. Sha, J. Wu, B. Paul, Y. Zhao, P. Mathews, Z. Li, J. Norris, E. Wang, D. P. McDonnell, Y. Kang, PPAR agonists attenuate lenalidomide's anti-myeloma activity in vitro and in vivo, Cancer Lett. 545 (2022), 215832.

[58] L. Ng, K. Nichols, K. O'Rourke, A. Maslen, G.M. Kirby, Repression of human GSTA1 by interleukin-1beta is mediated by variant hepatic nuclear factor-1C, Mol. Pharmacol. 71 (2007) 201–208.

[59] A. Kalbasi, A. Ribas, Tumour-intrinsic resistance to immune checkpoint blockade, Nat. Rev. Immunol. 20 (2020) 25–39.

[60] G.P.F. Nader, S. Aguera-Gonzalez, F. Routet, M. Gratia, M. Maurin, V. Cancila, C. Cadart, A. Palamidessi, R.N. Ramos, M. San Roman, M. Gentili, A. Yamada, A. Williart, C. Lodillinsky, E. Lagoutte, C. Villard, J.L. Viovy, C. Tripodo, J. Galon, G. Scita, N. Manel, P. Chavrier, M. Piel, Compromised nuclear envelope integrity drives TREX1-dependent DNA damage and tumor cell invasion, Cell 184 (2021) 5230–5246, e5222.

[61] L. Deng, H. Liang, M. Xu, X. Yang, B. Burnette, A. Arina, X.D. Li, H. Mauceri, M. Beckett, T. Darga, X. Huang, T.F. Gajewski, Z.J. Chen, Y.X. Fu, R. R. Weichselbaum, STING-dependent cytosolic DNA sensing promotes radiation-induced type I interferon-dependent antitumor immunity in immunogenic tumors, Immunity 41 (2014) 843–852.

[62] L. Ding, H.J. Kim, Q. Wang, M. Kearns, T. Jiang, C.E. Ohlson, B.B. Li, S. Xie, J. F. Liu, E.H. Stover, B.E. Howitt, R.T. Bronson, S. Lazo, T.M. Roberts, G.J. Freeman, P.A. Konstantinopoulos, U.A. Matulonis, J.J. Zhao, PARP inhibition elicits STING-dependent antitumor immunity in brca1-deficient ovarian cancer, Cell Rep. 25 (2018) 2972–2980, e2975.

[63] Z. Zhang, X. Liu, D. Chen, J. Yu, Radiotherapy combined with immunotherapy: the dawn of cancer treatment, Signal Transduct. Targeted Ther. 7 (2022) 258.

[64] C. Conche, F. Finkelmeier, M. Pešić, A.M. Nicolas, T.W. Böttger, K.B. Kennel, D. Denk, F. Ceteci, K. Mohs, E. Engel, Ö. Canli, Y. Dabiri, K.-H. Peiffer, S. Zeuzem, G. Salinas, T. Longerich, H. Yang, F.R. Greten, Combining ferroptosis induction with MDSC blockade renders primary tumours and metastases in liver sensitive to immune checkpoint blockade, Gut 72 (2023) 1774–1782.

[65] T. Hoch, D. Schulz, N. Eling, J.M. Gomez, M.P. Levesque, B. Bodenmiller, Multiplexed imaging mass cytometry of the chemokine milieus in melanoma characterizes features of the response to immunotherapy, Sci Immunol 7 (2022), eabk1692.

[66] Z. Shi, J. Shen, J. Qiu, Q. Zhao, K. Hua, H. Wang, CXCL10 potentiates immune checkpoint blockade therapy in homologous recombination-deficient tumors, Theranostics 11 (2021) 7175–7187.

[67] X. Li, M. Lu, M. Yuan, J. Ye, W. Zhang, L. Xu, X. Wu, B. Hui, Y. Yang, B. Wei, C. Guo, M. Wei, J. Dong, X. Wu, Y. Gu, CXCL10-armed oncolytic adenovirus promotes tumor-infiltrating T-cell chemotaxis to enhance anti-PD-1 therapy, OncoImmunology 11 (2022), 2118210.

[68] X. Han, Y. Wang, J. Sun, T. Tan, X. Cai, P. Lin, Y. Tan, B. Zheng, B. Wang, J. Wang, L. Xu, Z. Yu, Q. Xu, X. Wu, Y. Gu, Role of CXCR3 signaling in response to anti-PD-1 therapy, EBioMedicine 48 (2019) 169–177.

[69] J. Li, J. Wang, W. Zhou, S. Zhang, Y. Le, R. He, Downregulation of BRAF-activated non-coding RNA suppresses the proliferation, migration and invasion, and induces apoptosis of hepatocellular carcinoma cells, Oncol. Lett. 14 (2017) 4751–4757.

[70] J. Yuan, T. Lv, J. Yang, Z. Wu, L. Yan, J. Yang, Y. Shi, L. Jiang, The lipid transporter HDLBP promotes hepatocellular carcinoma metastasis through BRAF-dependent epithelial-mesenchymal transition, Cancer Lett. 549 (2022), 215921.

[70] M. Caraglia, G. Giuberti, M. Marra, R. Addeo, L. Montella, M. Murolo, P. Sperlongano, B. Vincenzi, S. Naviglio, S.D. Prete, A. Abbruzzese, P. Stiuso, Oxidative stress and ERK1/2 phosphorylation as predictors of outcome in hepatocellular carcinoma patients treated with sorafenib plus octreotide LAR, Cell Death Dis. 2 (2011) e150.